Mechanical Systems and Signal Processing 184 (2023) 109636

Contents lists available at ScienceDirect

Mechanical Systems and Signal Processing

journal homepage: www.elsevier.com/locate/ymssp

Viscoelastic free vibration analysis of in-plane functionally graded orthotropic plates integrated with piezoelectric sensors: Time-dependent 3D analytical solutions

A. Singh [a], S. Naskar [b], P. Kumari [c], T. Mukhopadhyay [a,*]

[a] Department of Aerospace Engineering, Indian Institute of Technology Kanpur, Kanpur, India
[b] Faculty of Engineering and Physical Sciences, University of Southampton, Southampton, UK
[c] Department of Mechanical Engineering, Indian Institute of Technology Guwahati, Guwahati, India

ARTICLE INFO

Communicated by A. Morassi

Keywords:
Extended Kantorovich method for dynamic analysis
Time-domain viscoelastic analysis
Smart functionally graded materials
Three-dimensional solution for piezo-embedded plates

ABSTRACT

This paper proposes an accurate three-dimensional framework for elastic and viscoelastic free vibration investigation of in-plane functionally graded (IPFG) orthotropic rectangular plates integrated with piezoelectric sensory layers. The developed analytical framework is capable of considering layer-wise unidirectional linear functional gradation in both stiffness and density of the orthotropic composite layers. 3D piezoelasticity-based governing equations of motion are formulated in mixed form by employing Hamilton's principle, and further solved analytically for Levy-type support conditions using the power-series-based extended Kantorovich method (EKM) jointly with Fourier series. The displacements, stresses, and electrical variables (electric field and electric potential) are solved as the primary variables that ensure the point-wise interlayer continuity and electro-mechanical support conditions. The viscoelastic property of the orthotropic interlayer is defined by employing Biot model, which is similar to the standard linear viscoelastic model. The correctness and efficacy of the present mathematical model are established by comparing the present numerical results with published literature and 3D finite element results, obtained by utilizing user material subroutine in the commercial FE software ABAQUS. An extensive numerical study is performed for various configurations and thickness ratios to investigate the influences of in-plane gradation, viscoelasticity and their coupled effects on the free-vibration response of hybrid laminated plates. It is found that in-plane gradation of stiffness and density remarkably alters the flexural frequencies and corresponding mode shapes of the hybrid intelligent rectangular plates. The flexural frequencies and stresses in the plate can be modified by selecting suitable grading indexes. Another interesting observation is that the in-plane gradation shows a considerably less effect on the electrical response of piezoelectric layers, which can play a vital role in the design of sensors and actuators for dynamic applications. Further, the numerical study demonstrates a potential time-dependent structural behaviour based on the present viscoelastic modelling. The consideration of viscoelasticity could be crucial for analysing the mechanical behaviour of a wide range of polymer composites more realistically and for prospective temporal programming in smart structural systems by exploiting the viscoelastic effect. Although the present analytical solution has been proposed for the free-vibration investigation of smart in-plane functionally graded (IPFG) viscoelastic plates, it can also be utilized directly to analyze the symmetric and asymmetric laminated piezoelectric smart plates with constant properties.

* Corresponding author.
E-mail address: tanmoy@iitk.ac.in (T. Mukhopadhyay).

https://doi.org/10.1016/j.ymssp.2022.109636
Received 12 January 2022; Received in revised form 21 July 2022; Accepted 28 July 2022
Available online 2 September 2022

1. Introduction

In the past decade, functionally graded materials have been widely explored for several engineering applications in the aerospace, civil, mechanical, and biomedical fields due to their superior mechanical and thermal properties [1]. Such materials give freedom to the designers for tailoring the mechanical properties of structures like stiffness, density, and thermal resistance along particular directions according to the operational requirements. This is achieved by introducing gradation in the material properties along that particular direction. However, it makes the computational analysis of such structures more complicated because their governing equations involve some variable coefficients, which are the functions of coordinate along which the gradation is considered (unlike conventional isotropic and composite plates). Hence, the structural problem of functionally graded structure cannot be solved by using the traditional methods proposed for the conventional structural problems [2]. Hence, more efficient and dedicated solution approaches are required for the accurate determination of structural behaviour of functionally graded structures under dynamic and static conditions, which is a prime focus of the present work.

A significant number of mathematical models have been developed for bending, fracture and natural frequency investigation of functionally graded beams, rectangular plates, and shell structures. An extensive review of the work related to functionally graded structures, presented by Byrd [3], Wu et al. [4] and Swaminathan et al. [5], suggests that in most of the studies through-thickness gradation of properties is considered following deterministic and stochastic frameworks [6–10]. However, over the last few years, the focus is getting diverted towards the in-plane and multidirectional functionally graded structures because it gives more freedom to control the material properties of thin structures for meeting application-specific demands, such as specific stiffness, strength, impact and thermal resistance, high fatigue strength, corrosion resistance, and acoustic properties [4]. In this context, Leissa and Martin [11] probed the buckling and natural frequency response of thin rectangular composite plates having in-plane graded properties and proved that desired buckling load and fundamental frequencies can be obtained effectively by controlling the gradation parameters of material along an in-plane direction.

Most of the analytical solutions for in-plane graded or multidirectional functionally graded plates published in the literature are based on two-dimensional (2D) theories of plates. For example, Tomar et al. [12] developed classical plate theory based 2D analytical solution for natural frequency investigation of isotropic functionally graded panels (length of the plate along is considered infinite along y-direction) employing Frobenius series. In this work, elastic modulus and density of the flat panel are taken exponentially graded along the axial (x) direction. Fares and Zenkour [13] have employed higher-order plate theory (HPT), first-order plate theory (FPT), and classical plate theory (CPT) to develop 2D analytical solutions for natural frequency and buckling investigation of multidirectional functionally graded orthotropic rectangular plates. They found that the index of gradation significantly affects the buckling and free vibration response of plate. Fourier series approach along with particular integration method has been utilized by Liu et al. [14] to solve the variable coefficient ordinary differential equation and they obtained classical plate theory (CPT) based solution for natural frequency analysis of in-plane functionally graded rectangular plates under Levy-type support condition. In their paper, they concluded that the desired natural frequencies can be attained by adjusting grading indexes. Yu et al. [15] have used the Whittaker technique for solving the fourth-order variable coefficients governing equation to obtain an analytical solution for flexural analysis of the thin in-plane graded isotropic plates of rectangular shape subjected to Levy-type end conditions. Recently, Amirpour et al. [16] provided HSDT-based analytical solutions for flexural investigation of in-plane functionally graded isotropic rectangular plates. In the literature, mostly 2D analytical solutions have been presented so far that belong to specific type of mechanical end conditions, like simply-supported or Levy-type support conditions. The governing equations involved in analysis are higher-order ODEs that have variable coefficients and to solve them in analytically for arbitrary boundary conditions is computationally difficult. Thus, some researchers employed numerical approaches to obtain reliable approximate two-dimensional solutions for in-plane multidirectional gradation in rectangular plates. Numerical solutions for non-classical boundary conditions are developed using the higher-order shear deformation theory [17–19] and the classical plate theories (CPT) [20–25]. Recently, Xue et al. [26] reported an isogeometric numerical solution for natural frequency investigation of IPFG plates by utilizing a refined plate theory and also extended this solution to obtain a FSDT-based numerical solution for modal investigation of circular, square, and rectangular porous FGM plates having porosity gradation along the in-plane and thickness directions. Utilizing Rayleigh–Ritz and Bolotin's method, Loja and Barbosa [27] proposed a 2D numerical solution based on classical plate theory for natural frequency and dynamic instability investigation of in-plane functionally graded thin plates.

Although it is found that the higher-order theory-based 2D solutions are adequate and reliable in obtaining the global response of thinner orthotropic plates, the accuracy of 2D solutions significantly reduces as the plate becomes thicker [28] and 2D theory-based results are not reliable for higher modes [28]. In 3D elasticity solutions, no pre-assumptions are adopted in the distribution of deformations and stresses. Both stresses and strains are solved as primary variables. Hence, the 3D solution of plates achieves high accuracy and is always preferred for bench-marking purposes, including accurate prediction of stresses near edges (the variation of stresses in the vicinity of edges is highly non-linear). In this direction, Lü et al. [29] reported a 3D semi-analytical solution for multidirectional graded Levy-type plate by using differential quadrature method based state-space approach (SSDQM). The stiffness of the rectangular plate was assumed exponentially graded along the axial (x) and thickness (z) directions. This analysis shows that the behaviour of rectangular plates is affected more by axial stiffness variation than through-thickness stiffness variation. Singh and Kumari developed a power series-based extended Kantorovich elasticity analytical approach for flexural analysis of in-plane functionally graded composite beams [30–33], panels [34,35], and rectangular plates [36]. Using a similar approach, Ravindran and Bhaskar [37] developed a 3D analytical approach for flexural analysis of IPFG simply-supported plates subjected to sinusoidal loading. They extended this approach further [38] for flexural analysis of simply-supported isotropic sandwich plates integrated with in-plane graded composite face sheets. Zhang et al. [39] have employed the scaled boundary finite element method (SBFEM)

to obtain a 3D semi-analytical solution for the flexural investigation of in-plane functionally graded (IPFG) isotropic rectangular plates. Singh and Kumari [40] recently presented a 3D analytical model for natural frequency modal analysis of orthotropic IPFG rectangular plates.

Some researchers have also explored pure numerical approaches to analyze the IPFG plates under static and dynamic conditions. The graded finite element-based numerical technique has been developed by Asemi et al. [41] for flexural investigation of bidirectional functionally graded plates. Xiang et al. [42] utilized this recently developed scaled boundary finite element method to obtain a 3D solution for buckling and natural frequency of the IPFG isotropic rectangular plates subjected to Navier and all-around clamped supports. The Chebyshev spectral approach has been utilized by Huang et al. [43] to obtain a numerical solution for static flexural and natural frequency analysis of orthotropic IPFG rectangular plates subjected to general support conditions.

Piezoelectric materials are getting increasingly employed in active response control and sensing applications as actuators and sensors due to their inherent property of producing a voltage in response to deformation and vice-versa [44–48]. When composite and FGM structures are integrated with piezoelectric sensors and actuators, their behaviours become very complex due to electro-mechanical coupling [49]. Due to weak coupling between elastic and electric parameters, the electrical response of active smart layers is very sensitive to internal or external factors such as internal imperfection or defects, external loading, etc. Moreover, when smart materials are used with FGM structure, the gradation of properties makes its response even more complex. Hence, efficient and reliable solutions are required to analyze the smart functionally graded structures accurately. A thorough review of the literature on functionally graded smart plates reveals that the through-thickness gradation of properties is commonly considered [50–54]. Only a few papers have been reported for in-plane functionally graded (IFGP) smart structures. Zhang et al. [55] utilized the precise integration method (PIM) in conjunction with the scaled boundary finite element method (SBFEM) to develop a semi-analytical model for static flexural investigation of magneto-electro-elastic IPFG plates. Later they extended this model to develop a semi-analytical framework for bending analysis of the in-plane and multidirectional graded piezoelectric plates [56] and also to natural frequency analysis of magneto-electro-elastic IPFG rectangular plates [57]. In all these solutions, only elastic displacements along the x, y and z-coordinates, magnetic potential and electric voltage are solved as the primary independent variables. To the best knowledge of the authors, no 3D analytical study has been presented to date for natural frequency investigation of in-plane functionally graded (IPFG) rectangular plates integrated with piezoelectric smart layers. Based on the extensive literature review, it is observed that benchmark 3D piezo-elasticity based analytical solutions are essential for in-plane functionally graded (IPFG) smart plates, which can serve as an accurate reference for future developments. Thus, this research work is carried out to fill this gap by providing a benchmark 3D mathematical model for IPFG plates.

Nowadays viscoelastic materials are widely used in vibration attenuation. Moreover, many of the polymers used in composites actually show a visco-elastic behaviour in their operational temperature regime. Besides accurate analysis of such structural systems, time-dependent viscoelastic behaviour can further be exploited for programming mechanical responses in smart structural systems. However, only a few works are reported for viscoelastic analysis with the coexistence of gradation and piezoelasticity. Zhang and Zheng [58] explored application of the Biot approach in analyzing the dynamic behaviour of viscoelastic composite structures. Hu and Wang [59] studied the effect of viscoelasticity on free vibration behaviour and transverse stresses with the help of Reddy's layerwise theory and showed that transverse stresses in the viscoelastic layer are the main factor that leads to delamination in lower modes. Mao et al. [60] studied the creep buckling and post-buckling behaviour of layered viscoelastic piezoelectric plates graded along thickness direction. Zenkour [61] studied the bending behaviour of elastic/ viscoelastic exponentially graded composite (EGC) rectangular sandwich plates using Illyushin's approximation methods. Wang et al. [62] used Kelvin–Voigt model for viscoelastic stability investigation of composite rectangular plates integrated with a smart piezoelectric layer and under a follower force. Alibeigloo [63] developed a 3D state-space model to study the effect of viscoelastic inter-layers on flexural and vibration response of simply-supported layered composite plates. Wu et al. [64] proposed a 3D elasticity-based analytical method for flexural investigation of simply supported layered plates having viscoelastic interlayers. Recently, Wang et al. [65] presented a 3D analytical model to investigate the time-dependent flexural response of exponential functionally graded laminated rectangular plates bonded by viscoelastic adhesive inter-layers. Apart from that, the application of viscoelastic layers in vibration damping is significantly explored in many recent studies [66–70].

Sun et al. [71] developed an inverse approach for calculating the frequency-dependent mechanical properties of viscoelastic medium using measured frequency response functions (FRFs). Grosso et al. [72] developed an experimental identification technique for calculating equivalent viscoelastic parameters of the model for layered thin-walled structures from the vibration data.

Based on the discussions presented in the preceding paragraphs, it becomes evident that development of an accurate 3D analytical solution approach for graded piezoelectric composites including the effect of viscoelasticity would have a wide range of impacts for analyzing and designing smart structural systems. In this article, we aim to propose an accurate 3D analytical framework for viscoelastic natural frequency investigation of in-plane functionally graded (IPFG) orthotropic rectangular plates integrated with piezoelectric layers [Advantages of the proposed mathematical model compared to others are listed in Remark 1, Appendix G (refer to the Supplementary material)]. Although the present analytical model is developed for the analysis of smart IPFG viscoelastic plates, it is also directly applicable for the investigation of laminated piezoelectric rectangular elastic and viscoelastic plates without any gradation. The present paper is organized chronologically in six sections as follows; the mathematical formulation of the 3D governing equations using the piezo-elasticity-based Hamilton's principle is explained in Section 2. In Section 3, the viscoelastic mathematical model is developed for obtaining effective viscoelastic properties of the viscoelastic layer in time domain. In Section 4, the extended Kantorovoch method together with the power series and Fourier series method is used to attain a solution in the approximated analytical form. Section 5 is dedicated to validation and numerical investigation. In section Section 5.1, numerical results are presented for elastic case and Section 5.2 is dedicated to viscoelastic analysis. Finally, the conclusions and interesting findings of the present study are summarized in the Section 6.

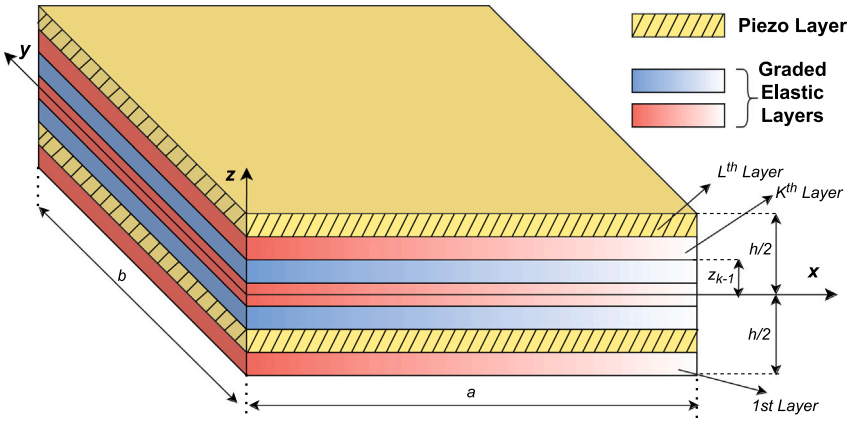

Fig. 1. Geometry of smart in-plane functionally graded (IPFG) plates.

2. 3D piezo-elasticity based formulation for modal analysis of hybrid FGM plates

A laminated in-plane functionally graded (IPFG) hybrid rectangular plate ($x \in (0, a)$, $z = -h/2,\ h/2$, $y \in (0, b)$) integrated with piezoelectric layers, as demonstrated in Fig. 1, is taken into consideration for the present numerical study. In such type of plates, the in-plane gradation of material properties in the elastic layers is helpful to control flexural frequency response of plate and at the same time piezoelectric layers act as sensor to sense the behaviour of plate under different gradation cases. The considered rectangular functionally graded plate consists of total L number of orthotropic IPFG layers and $\xi_1\ (= x/a)$, $\zeta^{(k)} = (z - z_{k-1})/t^{(k)}$ and $\xi_2\ (= y/b)$ are non-dimensionalized layer parameter defined for x, z (thickness) and y-direction, respectively. Here the non-dimensional parameters ξ_1 and ξ_2 are defined as global parameters which are valid for all layers. But $\zeta^{(k)}$ is local thickness parameter of layer defined for each kth layer and $t^{(k)}$ denotes the thickness of that kth layer, and z_k represents thickness coordinate parameter for the upper layer surface of that kth layer. These superscripts of layers may be excluded in the further mathematical expressions unless absolutely needed for better clarity.

The strain–displacement and the electrical field-potential relations for the 3D rectangular hybrid plate can be written as,

$$\begin{bmatrix}\epsilon_x\\ \epsilon_y\\ \epsilon_z\end{bmatrix} = \begin{bmatrix}u_{,x}\\ v_{,y}\\ w_{,z}\end{bmatrix}; \qquad \begin{bmatrix}\gamma_{yz}\\ \gamma_{zx}\\ \gamma_{xy}\end{bmatrix} = \begin{bmatrix}v_{,z} + w_{,y}\\ w_{,x} + u_{,z}\\ u_{,y} + v_{,x}\end{bmatrix}; \qquad \begin{bmatrix}E_x\\ E_y\\ E_z\end{bmatrix} = \begin{bmatrix}\phi_{,x}\\ \phi_{,y}\\ \phi_{,z}\end{bmatrix} \tag{1}$$

In these expressions ϵ_i represents normal strains and γ_{ij} represents shear strains of the plate, wherein w, v and u denote the displacement along z, y and x directions, respectively. Similarly, electric fields along x, y and z directions are designated by E_x, E_y and E_z, respectively. $\bar{\phi}$ denotes electric potential in the piezo-electric layer.

The 3D piezo-elasticity based linear constitutive equations for an orthotropic smart layer can be expressed as

$$\begin{aligned}
\epsilon_x &= s_{11}\sigma_x + s_{12}\sigma_y + s_{13}\sigma_z + d_{31}E_z\\
\epsilon_y &= s_{12}\sigma_x + s_{22}\sigma_y + s_{23}\sigma_z + d_{32}E_z\\
\epsilon_z &= s_{13}\sigma_x + s_{23}\sigma_y + s_{33}\sigma_z + d_{33}E_z\\
\gamma_{yz} &= s_{44}\tau_{yz} + d_{24}E_y\\
\gamma_{zx} &= s_{55}\tau_{zx} + d_{15}E_x\\
\gamma_{xy} &= s_{66}\tau_{xy}
\end{aligned} \tag{2}$$

$$\begin{aligned}
D_x &= d_{15}\tau_{zx} + \epsilon_{11}E_x\\
D_y &= d_{24}\tau_{yz} + \epsilon_{22}E_y\\
D_z &= d_{31}\sigma_x + d_{32}\sigma_y + d_{33}\sigma_z + \epsilon_{33}E_z
\end{aligned} \tag{3}$$

In above expressions, D_i, σ_i and τ_{ij} are the electric displacement, normal stress and shear stress components, respectively. The piezoelectric strain constants d_{ij}, dielectric permittivities ϵ_{ij} (at constant stress field) and elastic compliances s_{ij} are given in Appendix A of the supplementary material.

The expression of E_x, E_y and E_z in terms of D_x, D_y and D_z can be obtained from Eq. (3). After putting these expressions of E_x, E_y and E_z into Eq. (2), we obtain

$$\begin{aligned}
\epsilon_x &= \bar{s}_{11}\sigma_x + \bar{s}_{12}\sigma_y + \bar{s}_{13}\sigma_z + \bar{d}_{31}D_z, \qquad & \epsilon_y &= \bar{s}_{12}\sigma_x + \bar{s}_{22}\sigma_y + \bar{s}_{23}\sigma_z + \bar{d}_{32}D_z\\
\epsilon_z &= \bar{s}_{13}\sigma_x + \bar{s}_{23}\sigma_y + \bar{s}_{33}\sigma_z + \bar{d}_{33}D_z, \qquad & E_z &= -\bar{d}_{31}\sigma_x - \bar{d}_{32}\sigma_y - \bar{d}_{33}\sigma_z + \bar{\epsilon}_{33}D_z
\end{aligned} \tag{4}$$

$$\gamma_{yz} = \bar{s}_{44}\tau_{yz} + \bar{d}_{24}D_y, \quad \gamma_{zx} = \bar{s}_{55}\tau_{zx} + \bar{d}_{15}D_x, \quad E_x = \bar{\epsilon}_{11}D_x - \bar{d}_{15}\tau_{zx} \quad E_y = \bar{\epsilon}_{22}D_y - \bar{d}_{24}\tau_{yz}$$

where

$$\begin{aligned}
&\bar{\epsilon}_{33} = 1/\epsilon_{33}, \qquad \bar{s}_{ij} = s_{ij} - d_{3i}\bar{d}_{3j}, \quad \bar{d}_{3i} = d_{3i}/\epsilon_{33}, \qquad \text{for} \quad (i,j) = 1,2,3\\
&\bar{s}_{44} = s_{44} - d_{24}\bar{d}_{24}, \qquad \bar{s}_{55} = s_{55} - d_{15}\bar{d}_{15}, \qquad \bar{s}_{66} = s_{66}\\
&\bar{\epsilon}_{11} = 1/\epsilon_{11}, \qquad \bar{\epsilon}_{22} = 1/\epsilon_{22}, \qquad \bar{d}_{24} = d_{24}/\epsilon_{22}, \qquad \bar{d}_{15} = d_{15}/\epsilon_{11}.
\end{aligned}$$

These constitutive equations are valid for piezoelectric elastic layers having constant material properties.

For in-plane functionally graded layers, the elastic compliances and density of particular layer are considered to vary continuously and linearly along the (x) coordinate of the plate as [40,73]

$$\begin{aligned}
&\rho^m(\xi_1) = \rho(1+\delta_p\xi_1) = \rho + \hat{\rho}\\
&\bar{s}^m_{1j}(\xi_1) = \bar{s}_{1j}(1+\delta_1\xi_1) = \bar{s}_{1j} + \hat{s}_{1j} \quad \text{for} \quad j = 1,2,3;\\
&\bar{s}^m_{55}(\xi_1) = \bar{s}_{55}(1+\delta_2\xi_1) = \bar{s}_{55} + \hat{s}_{55}; \quad \bar{s}^m_{66} = \bar{s}_{66}(1+\delta_2\xi_1) = \bar{s}_{66} + \hat{s}_{66}
\end{aligned} \tag{5}$$

Here δ_p denotes gradation index for density, δ_1 and δ_2 denote gradation indexes correspond to Young's and shear modulus, respectively. These gradation parameters (δ_p, δ_1 and δ_2) can have any positive and negative numerical value. This type of gradation is considered to provide flexibility to present mathematical model in considering different kind of variation in material properties. Therefore, the present mathematical model can be used for graded cases in which variation of material properties is introduced intentionally to achieve specific structural behaviour. Additionally, this formulation can also be used for degradation cases in which elastic properties of some specific layers may deteriorate due to dispersion of moisture or some chemicals such as hydrogen or due to periodic exposure to heat etc. Therefore, for in-plane functionally graded layers, Eq. (4) are modified and can be expressed as,

$$\begin{aligned}
&\epsilon_x = (\bar{s}_{11} + \hat{s}_{11})\sigma_x + (\bar{s}_{12} + \hat{s}_{12})\sigma_y + (\bar{s}_{13} + \hat{s}_{13})\sigma_z + \bar{d}_{31}D_z\\
&\epsilon_y = (\bar{s}_{12} + \hat{s}_{12})\sigma_x + \bar{s}_{22}\sigma_y + \bar{s}_{23}\sigma_z + \bar{d}_{32}D_z\\
&\epsilon_z = (\bar{s}_{13} + \hat{s}_{13})\sigma_x + \bar{s}_{23}\sigma_y + \bar{s}_{33}\sigma_z + \bar{d}_{33}D_z\\
&E_z = -\bar{d}_{31}\sigma_x - \bar{d}_{32}\sigma_y - \bar{d}_{33}\sigma_z + \bar{\epsilon}_{33}D_z\\
&\gamma_{yz} = (\bar{s}_{44} + \hat{s}_{44})\tau_{yz} + \bar{d}_{24}D_y, \qquad \gamma_{zx} = (\bar{s}_{55} + \hat{s}_{55})\tau_{zx} + \bar{d}_{15}D_x\\
&E_x = \bar{\epsilon}_{11}D_x - \bar{d}_{15}\tau_{zx} \qquad E_y = \bar{\epsilon}_{22}D_y - \bar{d}_{24}\tau_{yz}
\end{aligned} \tag{6}$$

A 3D piezo-elasticity based extended Hamilton's principle in a mixed form, without any type of charge source and body force, can be expressed as,

$$\int_t\int_V [(\sigma_{ij,j} - \rho\ddot{u}_i)\delta u_i + (\varepsilon_{ij} - 0.5(u_{i,j} + u_{j,i}))\delta\sigma_{ij} + D_{i,i}\delta\phi - (E_i + \phi_{,i})\delta D_i]\mathrm{d}V\,\mathrm{d}t = 0, \tag{7}$$

where V is the volume ($a\times b\times h$) of the three-dimensional plate under consideration and i = 1, 2, 3 represent the x, y, z coordinate, respectively. Hence, $u_1 = u$, $u_2 = v$, $u_3 = w$, $\varepsilon_1 = \varepsilon_x$, $\varepsilon_2 = \varepsilon_y$, $\varepsilon_3 = \varepsilon_z$, $\varepsilon_{12} = \gamma_{xy}$, $\varepsilon_{23} = \gamma_{yz}$, $\varepsilon_{31} = \gamma_{zx}$, $\sigma_1 = \sigma_x$, $\sigma_2 = \sigma_y$, $\sigma_3 = \sigma_z$, $\sigma_{12} = \tau_{xy}$, $\sigma_{23} = \tau_{yz}$, $\sigma_{31} = \tau_{zx}$, $E_1 = E_x$, $E_2 = E_y$, $E_3 = E_z$, $D_1 = D_x$, $D_2 = D_y$ and $D_3 = D_z$. Substituting the expressions of the electric components and strains from Eqs. (6) and (1) into Eq. (7) yields

$$\begin{aligned}
&\int_t\int_a\int_b\int_h [\delta u\{\tau_{xz,z} + \sigma_{x,x} + \tau_{xy,y} - (\rho+\hat{\rho})\ddot{u}\} + \delta v\{\tau_{yz,z} + \tau_{xy,x} + \sigma_{y,y} - (\rho+\hat{\rho})\ddot{v}\} + \delta w\{\sigma_{z,z} + \tau_{zx,x}\\
&+ \tau_{yz,y} - (\rho+\hat{\rho})\ddot{w}\} + \delta\phi(D_{x,x} + D_{y,y} + D_{z,z}) + \delta\sigma_x\{(\bar{s}_{11} + \hat{s}_{11})\sigma_x + (\bar{s}_{12} + \hat{s}_{12})\sigma_y + (\bar{s}_{13} + \hat{s}_{13})\sigma_z\\
&+ \bar{d}_{31}D_z - u_{,x}\} + \delta\sigma_y\{(\bar{s}_{12} + \hat{s}_{12})\sigma_x + \bar{s}_{22}\sigma_y + \bar{s}_{23}\sigma_z + \bar{d}_{32}D_z - v_{,y}\} - \delta\sigma_z\{w_{,z} - (\bar{s}_{13} + \hat{s}_{13})\sigma_x\\
&- \bar{s}_{23}\sigma_y - \bar{s}_{33}\sigma_z - \bar{d}_{33}D_z\} - \delta\tau_{yz}(v_{,z} + w_{,y} - \bar{s}_{44}\tau_{yz} - \bar{d}_{24}D_y) - \delta\tau_{zx}\{u_{,z} + w_{,x} - (\bar{s}_{55} + \hat{s}_{55})\tau_{zx}\\
&- \bar{d}_{15}D_x\} + \delta\tau_{xy}\{(\bar{s}_{66} + \hat{s}_{66})\tau_{xy} - v_{,x} - u_{,y}\} - \delta D_x(\phi_{,x} + \bar{\epsilon}_{11}D_x - \bar{d}_{15}\tau_{zx}) - \delta D_y(\phi_{,y} + \bar{\epsilon}_{22}D_y\\
&- \bar{d}_{24}\tau_{yz}) - \delta D_z(\phi_{,z} - \bar{d}_{31}\sigma_x - \bar{d}_{32}\sigma_y - \bar{d}_{33}\sigma_z + \bar{\epsilon}_{33}D_z)]\,\mathrm{d}z\,\mathrm{d}y\,\mathrm{d}x\,\mathrm{d}t = 0, \quad \forall\ \delta u_i,\ \delta\phi,\ \delta\sigma_i,\ \delta\tau_{ij},\ \delta D_i
\end{aligned} \tag{8}$$

The exterior surfaces of the plate (bottom-most and top-most surface) are shear traction free. Therefore, the boundary conditions of exterior surface at $z = \pm h/2$ can be expressed as,

$$\text{at} \quad z = \pm h/2: \quad \tau_{yz} = 0, \quad \tau_{zx} = 0, \quad \sigma_z = 0 \tag{9}$$

If top or bottom surface is subjected to close-circuit (CC) condition then ϕ is prescribed. For open circuit condition D_z is prescribed. Therefore, for close-circuit surface $\phi(x,y) = 0$ and for open-circuit surface $D_z(x,y) = 0$. For multilayered FGM plates, perfect bonding is assumed between different functionally graded layers. Therefore, following continuity condition is satisfied at each internal surface between kth and $(k+1)$th layers

$$[(u,\ v,\ w,\ \phi,\ D_z,\ \sigma_z,\ \tau_{yz},\ \tau_{zx})|_{\zeta=1}]^{(k)} = [(u,\ v,\ w,\ \phi,\ D_z,\ \sigma_z,\ \tau_{yz},\ \tau_{zx})|_{\zeta=0}]^{(k+1)} \quad \text{for} \quad k = 1,\ldots,L-1 \tag{10}$$

In the present mathematical model, interfaces of smart piezoelectric layers with IPFG elastic substrate are considered as grounded ($\phi = 0$) for better sensing. Note that when the interfaces between the piezoelectric layers and the elastic substrate are made grounded,

the maximum potential difference will appear on top of the piezoelectric layer on the application of force. This is easier to evaluate accurately and effectively, which makes sensing better by easing the potential evaluation. Therefore, D_z becomes discontinuous at these interfaces. Subsequently, the continuity condition given in Eq. (10) is changed to $[\phi|_{\zeta=1}]^{(n_q)} = 0$ *i.e.* $q = 1, \ldots, L_a$, where L_a expresses the piezo-elastic layer interface where actuation electric voltage/potential is prescribed.

The present investigation is for Levy-type boundary conditions, hence the two opposite ends of the IPFG laminate smart plate along y-direction (at $y = 0$ and $y = b$) are always considered under simply-supported and close-circuit conditions. Thus, $\sigma_y = w = u = 0$ at $y = 0$ and b for all x, z of that plane. The other two opposite edges of hybrid FGM plate can have any type of mechanical and electrical support conditions. The mechanical support conditions at the edges $\xi_1 = 0$ and 1 can be clamped ($w = u = v = 0$), free ($\sigma_x = \tau_{xz} = \tau_{xy} = 0$) or simply-supported ($\sigma_x = w = v = 0$) at each point of corresponding $y - z$ plane. The ends of piezo-electric layers can have closed circuit (CC) condition ($\phi = 0$) or open circuit (OC) condition ($D_x = 0$).

3. Formulation for viscoelastic analysis

First classical elasticity analysis is performed in which instantaneous stresses within a material are considered only function of instantaneous strains, as presented in the preceding section. Now to implement viscoelasticity of material in the analysis, instantaneous stresses are assumed as a function of strains history by employing linear viscoelastic model. In a simplified linear viscoelastic mathematical model, the stress $\sigma(t)$ at any point within the structure is a function of time and can be written in the form of convolution integral on the kernel function [74] as

$$\sigma_t(t) = g_t(t) \circledast \varepsilon(t) \tag{11}$$

In above equation, $t \in \mathbb{R}^+$ is the dimensionless time parameter, $\sigma(t)$ and $\varepsilon(t)$ are representing time-dependent stress and strain, respectively. Here, it is assumed that the strain is zero for negative times. Hence, the initial strain is $\varepsilon_t = 0$ for $t < 0$ and g_t is the kernel or memory function. Causality requirements enforce g_t to be a causal function *i.e.* , it vanishes for $t < 0$; $g_t(t) = 0, \forall t < 0$. This approach of deriving time-dependent stress equations in the context of linear viscoelasticity is known as the hereditary approach, which gives greater freedom in constructing viscoelastic models as compared to the differential approach that only relies on the concepts of certain springs and dashpots combinations. Hence, time-dependent stress–strain relationship of Eq. (11) can directly be used for dynamic investigation of a solid viscoelastic body. Such as, in case of its implementation to uniform bar, Eq. (11) must be multiplied by its cross-section area which give the displacement and force rate (or velocity). In Eq. (11), $g_t(t)$ is also known as 'relaxation function', 'after-effect function' or 'hereditary function' in the context of different fields. Generally for the simplicity, the kernel function ($g_t(t)$) is usually described in the frequency domain which is also known as Laplace domain form. Hence, Laplace transformation of Eq. (11) converts it into frequency domain which can be expressed as

$$\bar{\sigma}_s(s_L) = s_L \bar{G}_s(s_L) \bar{\varepsilon}_s(s_L) \tag{12}$$

Here $s_L \in \mathbb{C}$ represents complex Laplace domain parameter. The parameters $\bar{\sigma}_s(s_L)$, $\bar{G}_s(s_L)$ and $\bar{\varepsilon}_s(s_L)$ are representing the corresponding Laplace transformation of $\sigma_t(t)$, $g_t(t)$ and $\varepsilon_t(t)$. The kernel function $g_t(t)$ can be constructed by two generally used methods one is approximation based mathematical approach and the other is general mathematical approach.

3.1. Construction of the kernel function using approximation based mathematical approach

In the approximation based mathematical approach, different combinations of springs and dashpots are used to obtain kernel function for viscoelastic constitutive relationship. Though a variety of springs and dashpots based models can be constructed by considering different arrangements, but for viscoelastic analysis of solid body generally four models [75,76] are used which are known as Maxwell viscoelastic model, Voigt viscoelastic model, Standard linear viscoelastic model and Generalized Maxwell viscoelastic model, as shown in Fig. 2. Here, Dirac delta function $\delta(t)$ and unit step function $\mathbb{U}(t)$ are defined as below

$$\mathbb{U}(t) = 1 \quad \text{if} \quad t \geq 0, \qquad \text{and} \qquad 0 \quad \text{if} \quad t < 0. \tag{13}$$

$$\delta(t) \circledast f_t(t) = f_t(t) \tag{14}$$

Here, $\delta(t)$ represents the Dirac delta function and $f_t(t)$ continuous generalized function. Dirac's delta $\delta(t)$ distribution represents the unit impulse function which is a generalized function or distribution over the real numbers [77,78]. Based on these assumptions, the viscoelastic kernel function ($g_t(t)$) for the four models can be expressed [74–76] as

- *Maxwell viscoelastic model:*

$$g_t(t) = \mu e^{-(\mu/\eta)t} \mathbb{U}(t) \tag{15}$$

- *Voigt viscoelastic model:*

$$g_t(t) = \eta \delta(t) + \mu \mathbb{U}(t) \tag{16}$$

- *Standard linear model:*

$$g_t(t) = E_R \left[1 - (1 - \frac{\tau_\sigma}{\tau_{\bar{\varepsilon}_s}}) e^{-t/\tau_{\bar{\varepsilon}_s}} \right] \mathbb{U}(t) \tag{17}$$

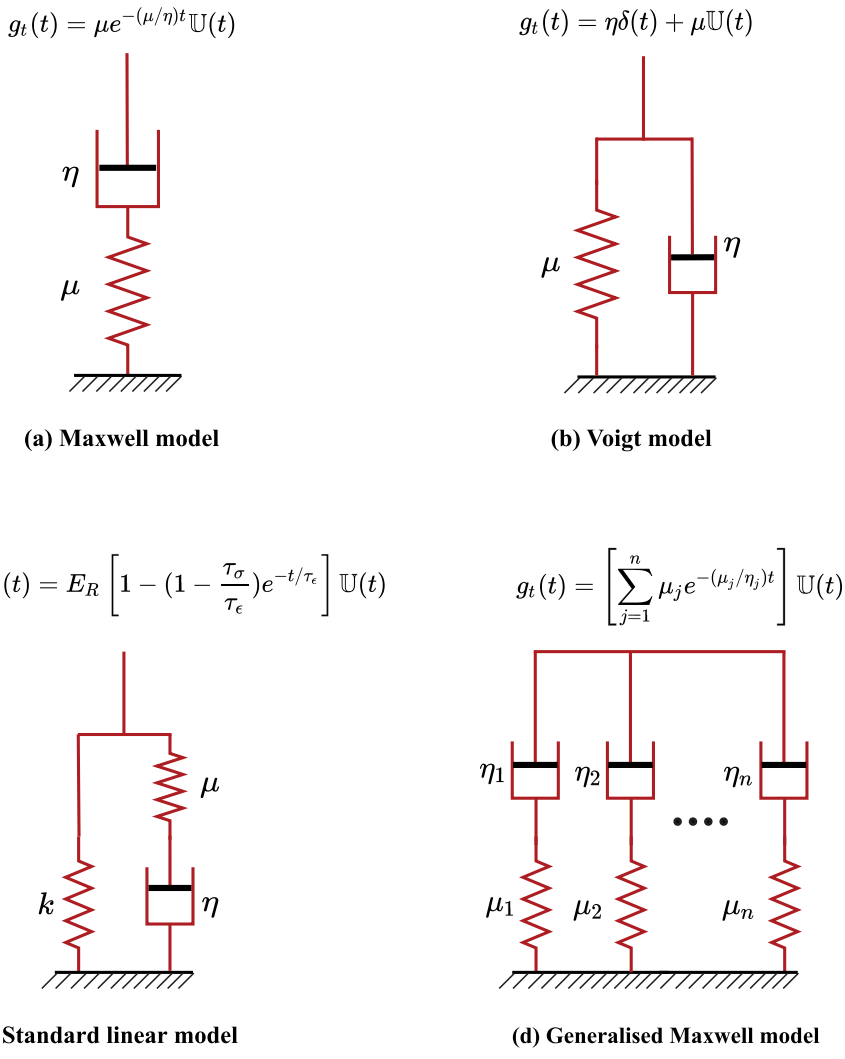

Fig. 2. Representation of viscoelastic materials models using springs and dashpots arrangement.

- *Generalized Maxwell viscoelastic model:*

$$g_t(t) = \left[\sum_{j=1}^{n} \mu_j e^{-(\mu_j/\eta_j)t}\right]\mathbb{U}(t) \tag{18}$$

This models is also called as the Prony series viscoelastic model.

These functions are obtained by assuming the equilibrium of different forces coming from stretching of the dashpots and springs as given in Fig. 2. In these functions, t is time, $\sigma(t)$ is stress, $\varepsilon(t)$ is strain of system, η is viscosity parameter of material represented by a purely viscous damper in the dashpots–springs system, μ is elastic stiffness parameter of material represented by a purely elastic spring in the dashpots–springs system, τ denotes relaxation time constant and E_R represents relaxation modulus.

3.2. Mathematical depiction of the kernel function in the frequency domain

The kernel function $g_t(t)$ in Eq. (12) can also be represented in the frequency (ω_s) state. It is a complex function which can be denoted as,

$$\bar{G}_s(\omega_s) = \bar{G}_s(\imath\omega_s) = G_s(\omega_s) \tag{19}$$

Here $\omega_s \in \mathbb{R}^+$ represents the frequency of Laplace domain signal. The complex function $G_s(\omega_s)$ can be split into real and imaginary part and can be also represented in term of amplitude and phase angle as,

$$G_s(\omega_s) = G'_s(\omega_s) + \imath G''_s(\omega_s) = |G_s(\omega_s)|e^{\imath\phi_s(\omega_s)} \tag{20}$$

Table 1
Representation of complex elasticity modulus for different viscoelastic material models in the Laplace or frequency domain.

Viscoelastic model	Complex elasticity modules
Biot model [82]	$G_s(\omega_s) = G_{s0} + \sum_{k=1}^{n} \frac{a_k \iota\omega_s}{\iota\omega_s + b_k}$
Fractional derivative [83]	$G_s(\omega_s) = \frac{G_{s0} + G_{s\infty}(\iota\omega_s\tau)^{\beta}}{1+(\iota\omega_s\tau)^{\beta}}$
ADF [84]	$G_s(\omega_s) = G_{s0}\left[1 + \sum_{k=1}^{n} \Delta_k \frac{\omega_s^2 + \iota\omega_s\Omega_{s_k}}{\omega_s^2 + \Omega_{s_k}^2}\right]$
GHM [85]	$G_s(\omega_s) = G_{s0}\left[1 + \sum_k \alpha_k \frac{-\omega_s^2 + 2\iota\xi_k\omega_{s_k}\omega_s}{-\omega_s^2 + 2\iota\xi_k\omega_{s_k}\omega_s + \omega_{s_k}^2}\right]$
Step-function [86]	$G_s(\omega_s) = G_{s0}\left[1 + \eta\frac{1-e^{-\omega_s t_0}}{\omega_s t_0}\right]$
Half cosine model [86]	$G_s(\omega_s) = G_{s0}\left[1 + \eta\frac{1+2(\omega_s t_0/\pi)^2 - e^{-\omega_s t_0}}{1+2(\omega_s t_0/\pi)^2}\right]$
Gaussian model [87]	$G_s(\omega_s) = G_{s0}\left[1 + \eta\, e^{\omega_s^2/4\mu}\left\{1 - \mathrm{erf}\left(\frac{\omega_s}{2\sqrt{\mu}}\right)\right\}\right]$

Real part $G_s'(\omega_s)$ is known as storage moduli and imaginary part $G_s''(\omega_s)$ is known as loss moduli. The kernel function has one main restriction, which comes from the relationship between cause and effect that the reaction of the structure depends upon its loading history. The output of a function at any time depends on past and present values of input which is known as causality condition and causal system. A causal system (also known as a physical or non-anticipative system) is a system where the output depends on past and current inputs but not future inputs—i.e., the output $y(t_0)$ depends only on the input $x(t)$ for values of $t \leq t_0$ [78]. Therefore, according to the causality condition, the structure's reaction should depend upon its loading history. Further, the Kramers–Kronigrelation [78] defines the mathematical correlation between the imaginary and real parts of the complex elasticity modulus (complex modulus) [70,78]. Kramers–Kroniginterrelations show that the imaginary and real parts of complex elasticity modulus must be linked by a Hilbert transform duo and it could be written mathematically as

$$G_s'(\omega_s) = G_{s\infty} + \frac{2}{\pi}\int_0^{\infty} \frac{uG_s''(u_s)}{\omega_s^2 - u_s^2}\,\mathrm{d}u_s \tag{21}$$

$$G_s''(\omega_s) = \frac{2\omega_s}{\pi}\int_0^{\infty} \frac{G_s'(u_s)}{u_s^2 - \omega_s^2}\,\mathrm{d}u_s \tag{22}$$

where $G_{s\infty} = G_s(\omega_s \to \infty) \in \mathbb{R}$ represents unrelaxed modulus. The integral in the Eqs. (21) and (22) is evaluated in Cauchy's principal value sense near the singularity [78–80]. The behaviour of visco-elastic material in the present case is considered to correspond to various spring dashpot combinations. Therefore, the reference signal has come from the corresponding spring–dashpot oscillator, where the real and imaginary parts bear the meaning according to the conventional signal processing literature [70,78]. The equivalent relationships which is linking the modulus $|G_s'(\omega_s)|$ and the phase $\phi_s(\omega_s)$ of $G_s(\omega_s)$ can be expressed as [Remark 4 and 5, Appendix G (refer to the Supplementary material)],

$$\ln|G_s'(\omega_s)| = \ln|G_{s\infty}| + \frac{2}{\pi}\int_0^{\infty} \frac{u_s\phi_s(u_s)}{\omega_s^2 - u_s^2}\,\mathrm{d}u_s \tag{23}$$

$$\phi_s(\omega_s) = \frac{2\omega_s}{\pi}\int_0^{\infty} \frac{\ln|G_s(u_s)|}{u_s^2 - \omega_s^2}\,\mathrm{d}u_s \tag{24}$$

It is worth mentioning that the approximation based principle described above to drive complex elasticity modulus automatically satisfy these conditions. However, other functions are also there which can also satisfy these conditions. The determination of $G_s(\omega_s)$, which satisfy these conditions, through experimental measurements is also possible [78,81]. The most commonly used functions in literature are listed in Table 1.

3.3. Effective material properties of viscoelastic layers in the laminated plate

In this paper, it is considered that each Young's moduli E_i (E_1, E_2, E_3) and each shear moduli G_{ij} (G_{12}, G_{13}, G_{23}) of viscoelastic layer is modelled using viscoelastic properties. The Biot model (mentioned in Table 1) with only one term has been used for computational simplicity. Hence, complex elastic and shear modulus in frequency domain [74] can be expressed as

$$E_i(\omega_s) = (E_s)_i\left(1 + \bar{\varepsilon}_s\frac{\iota\omega_s}{\mu + \iota\omega_s}\right) \tag{25}$$

$$G_{ij}(\omega_s) = (G_s)_{ij}\left(1 + \bar{\varepsilon}_s\frac{\iota\omega_s}{\mu + \iota\omega_s}\right) \tag{26}$$

where E_i represents the elastic modulus of the orthotropic layers considering viscoelasticity and $(E_s)_i$ represents the elastic modulus in absence of viscoelasticity. Similarly, G_{ij} represents the shear modulus of the orthotropic layers when viscoelasticity is considered and $(G_s)_{ij}$ represents the shear modulus in absence of viscoelasticity. In these expressions, μ is the relaxation parameter and $\bar{\varepsilon}_s$ represents a constant defining the 'strength' of viscosity. The amplitude of complex elastic moduli and shear moduli [74] is given

by

$$|E_i(\omega_s)| = E_{si}\sqrt{\frac{\mu^2+\omega_s^2\left(1+\bar{\varepsilon}_s\right)^2}{\mu^2+\omega_s^2}} \tag{27}$$

$$|G_{ij}(\omega_s)| = G_{sij}\sqrt{\frac{\mu^2+\omega_s^2\left(1+\bar{\varepsilon}_s\right)^2}{\mu^2+\omega_s^2}} \tag{28}$$

The phase (ϕ_s) [74] of these complex elastic moduli and shear moduli are given by

$$\phi_s\left(E_i(\omega_s)\right) = \phi_s\left(G_{ij}(\omega_s)\right) = \tan^{-1}\left(\frac{\mu\bar{\varepsilon}_s\omega_s}{\mu^2+\omega_s^2(1+\bar{\varepsilon}_s)}\right) \tag{29}$$

The complex elastic and shear moduli have the various limiting properties which are providing critical insights for various special cases. These limiting properties are listed in Appendix B (refer to the Supplementary material).

3.3.1. Numerical transformation of frequency domain into the time domain

The objective of the present paper is to present the time-dependent viscoelastic behaviour. Therefore, once the Frequency (Laplace) domain solutions are obtained using the viscoelastic correspondence principle, as described in the preceding subsection, they are inverted back into the time domain. The Inversion of frequency domain data into the time-domain is performed by employing the computationally efficient inverse Fourier transform (IFFT) [88,89]. The physical interpretation of time signal into the Fourier transform can be expressed as

$$E_i(t) = \frac{1}{2\pi}\int_{-\infty}^{\infty} E_i(\omega_s)e^{\imath\omega_s t}\mathrm{d}\omega = \int_{-\infty}^{\infty} E_i(2\pi f_s)e^{2\pi\imath f_s t}\mathrm{d}f_s \tag{30}$$

$$G_{ij}(t) = \frac{1}{2\pi}\int_{-\infty}^{\infty} G_{ij}(\omega_s)e^{\imath\omega_s t}\mathrm{d}\omega = \int_{-\infty}^{\infty} G_{ij}(2\pi f_s)e^{2\pi\imath f_s t}\mathrm{d}f_s \tag{31}$$

Here, $E_i(t)$ and $G_{ij}(t)$ represent relaxation elastic and shear moduli for composite orthotropic layers. The physical interpretation of an equation indicates the act of establishing the relation between the physical quantities in the equation by expecting how the system will behave at extreme or normal conditions. It can involve some approximations of the equation. The main characteristics of materials with viscoelasticity are used to describe the stress relaxation of materials with time (t). The efficient determination of $E_i(t)$ and $G_{ij}(t)$ must accurately simulate the viscoelastic deformation and stress relaxation in the material. Since in the inversion, discrete numerical data of frequency domain is used rather than a continuous expression for computation convenience, the continuous inverse Fourier transform can be expressed by its discrete counterpart as,

$$E_i(t) = \sum_{n=-\infty}^{\infty} C_n^E e^{\imath 2\pi nt} \quad \text{and} \quad G_{ij}(t) = \sum_{n=-\infty}^{\infty} C_n^G e^{\imath 2\pi nt} \tag{32}$$

where coefficients C_n^E and C_n^G are given by,

$$C_n^E = |E_i(\omega_{s_n})|\, e^{\imath\phi\left(E(\omega_{s_n})\right)} \tag{33}$$

$$C_n^G = |G_{ij}(\omega_{s_n})|\, e^{\imath\phi\left(G(\omega_{s_n})\right)} \tag{34}$$

It shows that whether the signal is periodic or not, its time waveform can be represented in the form of amplitude $|E(\omega_{s_n})|$ and phase $\phi\left(E(\omega_{s_n})\right)$. For more information on the relationships between the continuous and discrete Fourier transform, one can refer to [90]. While inverting the frequency domain data into the time domain, all values (higher to lowest) of the parameter ω_s are considered. So the time domain signal shows oscillation at each time step and to smoothen this time signal Savitzky–Golay smoothing algorithm is used here.

4. EKM-Fourier series based analytical solution approach

In the present mathematical model both mechanical and electrical variables are considered as primary variables. Thus, the mechanical displacements variables (u, v, w), electrical variables (ϕ, D_x, D_y and D_z) and the stresses variables (σ_x, σ_y, σ_z, τ_{xy}, τ_{yz}, τ_{zx}) are functions of ξ_1, ξ_2, and ζ, and solved as primary variables using combination of extended Kantorovich method and Fourier series approach, as further explained in this section.

To obtain the solution for y-direction, Fourier series approach is utilized and solution is assumed in form of Fourier series in such a manner that it satisfies simply-supported end conditions ($\sigma_y = w = u = 0$ at edges $\xi_2 = 0, 1$) of y direction [Remark 3: Appendix G (supplementary material)],

$$\begin{aligned}\left[u,\, w,\, \sigma_x,\, \sigma_y,\, \sigma_z,\, \tau_{zx},\, \phi,\, D_x,\, D_z\right] &= \sum_{m=1}^{M_y}\left[(u,\, w,\, \sigma_x,\, \sigma_y,\, \sigma_z,\, \tau_{zx},\, \phi,\, D_x,\, D_z)_m\cos\omega t\right]\sin m\pi\xi_2\\ \left[v,\, \tau_{yz},\, \tau_{xy},\, D_y\right] &= \sum_{m=1}^{M_y}\left[(v,\, \tau_{yz},\, \tau_{xy},\, D_y)_m\cos\omega t\right]\cos m\pi\xi_2\end{aligned} \tag{35}$$

where M_y represents the number of term in Fourier series and $(\,)_m$ denotes the mth term of Fourier series, and it is the function of ξ_1 and ζ. The truncated Fourier series is used where truncation of series (no. of terms in Fourier series) is corresponding to the flexural vibration mode of y-directions. A rectangular plate can have infinite flexural vibration modes along any direction. Hence, for general case $M_y \to \infty$. However, as in engineering application, the interest is over finite number of fundamental modes, the series has usually finite number of terms depending on the vibration modes of interest. Further, we substitute these Fourier series assumption, given in Eq. (35), into the extended Hamilton's principle expressed in Eq. (8). It transforms Eq. (8) into the following form, due to the orthogonality of cosine and sine functions,

$$\begin{aligned}
&\int_t\int_a\int_h [\delta u_m\{\tau_{xz_m,z} + \sigma_{x_m,x} - \bar{m}\tau_{xy_m} - (\rho+\hat{\rho})\omega^2 u_m\} + \delta v_m(\tau_{yz_m,z} + \tau_{xy_m,x} + \bar{m}\sigma_{y_m} - (\rho+\hat{\rho})\omega^2 v_m)\\
&+ \delta w_m\{\sigma_{z_m,z} + \tau_{zx_m,x} - \bar{m}\tau_{yz_m} - (\rho+\hat{\rho})\omega^2 w_m\} + \delta\phi_m(D_{x_m,x} - \bar{m}D_{y_m} + D_{z_m,z}) + \delta\sigma_{x_m}((\bar{s}_{11}+\hat{s}_{11})\sigma_{x_m}\\
&+ (\bar{s}_{12}+\hat{s}_{12})\sigma_{y_m} + (\bar{s}_{13}+\hat{s}_{13})\sigma_{z_m} + \bar{d}_{31}D_{z_m} - u_{m,x}) + \delta\sigma_{y_m}((\bar{s}_{12}+\hat{s}_{12})\sigma_{x_m} + \bar{s}_{22}\sigma_{y_m} + \bar{s}_{23}\sigma_{z_m} + \bar{d}_{32}D_{z_m}\\
&+ \bar{m}v_m) - \delta\sigma_{z_m}(w_{m,z} - (\bar{s}_{13}+\hat{s}_{13})\sigma_{x_m} - \bar{s}_{23}\sigma_{y_m} - \bar{s}_{33}\sigma_{z_m} - \bar{d}_{33}D_{z_m}) - \delta\tau_{yz_m}(v_{m,z} + \bar{m}w_m - \bar{s}_{44}\tau_{yz_m}\\
&- \bar{d}_{24}D_{y_m}) - \delta\tau_{zx_m}(u_{m,z} + w_{m,x} - (\bar{s}_{55}+\hat{s}_{55})\tau_{zx_m} - \bar{d}_{15}D_{x_m}) + \delta\tau_{xy_m}((s_{66}+\hat{s}_{66})\tau_{xy_m} - v_{m,x} - \bar{m}u_m)\\
&- \delta D_{x_m}(\phi_{m,x} + \bar{e}_{11}D_{x_m} - \bar{d}_{15}\tau_{zx_m}) - \delta D_{y_m}(\bar{m}\phi_m + \bar{e}_{22}D_{y_m} - \bar{d}_{24}\tau_{yz_m}) - \delta D_{z_m}(\phi_{m,z} - \bar{d}_{31}\sigma_{x_m} - \bar{d}_{32}\sigma_{y_m}\\
&- \bar{d}_{33}\sigma_{z_m} + \bar{e}_{33}D_{z_m})]\mathrm{d}z\mathrm{d}x\mathrm{d}t = 0, \quad \forall \quad \delta u_{i_m}, \delta\phi_m, \delta\sigma_{i_m}, \delta\tau_{i_j m}, \delta D_{i_m} \qquad \text{where} \quad \bar{m} = m\pi/b
\end{aligned} \tag{36}$$

The above expression appears for every Fourier term. Now dependency of each variable is reduced and all primary field variables, $\mathbf{X} = \begin{bmatrix} u_m & v_m & w_m & \sigma_{x_m} & \sigma_{y_m} & \sigma_{z_m} & \tau_{xy_m} & \tau_{yz_m} & \tau_{zx_m} & \phi_m & D_{x_m} & D_{y_m} & D_{z_m} \end{bmatrix}^{\mathrm{T}}$ are function of ξ_1 (x-coordinate) and ζ (thickness coordinate) only. The solution along these two-directions (for x and z- direction) is obtained further by employing recently developed the multi-term extended Kantorovich method [30,34,36,40,73,91]. The solution of X_l, lth variable $\mathbf{X}$, is assumed as the summation of n terms series containing products of two separable unknown functions $g_l^i(\zeta)$ and $f_l^i(\xi_1)$. Thus, the solution of each X_l variable can be expressed for the kth layer as,

$$X_{l_m}(\xi_1,\zeta) = \sum_{i=1}^{n} f_{l_m}^i(\xi_1) g_{l_m}^i(\zeta) \qquad \text{for} \quad l = 1,2,\ldots,13 \tag{37}$$

Here, $f_l^i(\xi_1)$ acts as global variable and is valid for all layers, while $g_l^i(\zeta)$ acts as local variable which is valid separately for every local kth layer. In the next sections, subscript 'm' is dropped from the mathematical expressions of $f_{l_m}^i$ and $g_{l_m}^i$ for convenience. Now, the solutions for unknown functions $g_l^i(\zeta)$ and $f_l^i(\xi_1)$ are obtained in two iterative steps.

4.1. First iterative step—solving functions $g_l^i(\zeta)$

In this iteration step, thickness function $g_l^i(\zeta)$ is solved. To start the first iteration step, $f_l^i(\xi_1)$ is assumed in sine and cosine form. In present EKM approach, the assumed initial functions need not satisfy any natural and essential boundary condition and it can be chosen arbitrarily. But for better convergence and to reduce the number of iteration for accurate solution, the $f_l^i(\xi_1)$ function is assumed corresponding to simply-supported boundary conditions of edges $\xi_1 = 0$ and 1. Hence, the initial functions $f_l^i(\xi_1)$ to the start the first step of iteration 1 can be assumed as $f_1^i(\xi_1) = f_7^i(\xi_1) = f_9^i(\xi_1) = f_{11}^i(\xi_1) = \cos i\pi\xi_1$; $f_2^i(\xi_1) = f_3^i(\xi_1) = f_4^i(\xi_1) = f_5^i(\xi_1) = f_6^i(\xi_1) = f_8^i(\xi_1) = f_{12}^i(\xi_1) = f_{13}^i(\xi_1) = \sin i\pi\xi_1$. Here, $f_1(\xi_1)$, $f_2(\xi_1)$, $f_3(\xi_1)$, $f_4(\xi_1)$, $f_5(\xi_1)$, $f_6(\xi_1)$, $f_7(\xi_1)$, $f_8(\xi_1)$, $f_9(\xi_1)$, $f_{10}(\xi_1)$, $f_{11}(\xi_1)$, $f_{12}(\xi_1)$ and $f_{13}(\xi_1)$ denote in-plane function for u, v, w, σ_x, σ_y, σ_z, τ_{xy}, τ_{yz}, τ_{zx}, ϕ, D_x, D_y and D_z, respectively. Now functions $g_l^i(\zeta)$ have to be solved in this iteration step, for which variation δX_l can be expressed as,

$$\delta X_l(\xi_1,\zeta) = \sum_{i=1}^{n} f_l^i(\xi_1)\delta g_l^i, \qquad l = 1,2,\ldots,13 \tag{38}$$

The functions $g_l^i(\zeta)$ can be divided into two parts $\bar{\mathbf{G}}$ and $\hat{\mathbf{G}}$. Here $\bar{\mathbf{G}}$ column vector is of dimension $8n$ and has the specific independent variables that comes in the interface condition, and mechanical/electrical boundary conditions at exterior surfaces (top and bottom) of hybrid FGM plate. The other $\hat{\mathbf{G}}$ column vector is of size $5n$ and has the other left over dependent variables,

$$\begin{aligned}
\bar{\mathbf{G}} &= \begin{bmatrix} g_1^1 \ldots g_1^n & g_2^1 \ldots g_2^n & g_3^1 \ldots g_3^n & g_6^1 \ldots g_6^n & g_8^1 \ldots g_8^n & g_9^1 \ldots g_9^n & g_{10}^1 \ldots g_{10}^n & g_{13}^1 \ldots g_{13}^n \end{bmatrix}^{\mathrm{T}}\\
\hat{\mathbf{G}} &= \begin{bmatrix} g_4^1 \ldots g_4^n & g_5^1 \ldots g_5^n & g_7^1 \ldots g_7^n & g_{11}^n \ldots g_{11}^n & g_{12}^n \ldots g_{12}^n \end{bmatrix}^{\mathrm{T}}
\end{aligned} \tag{39}$$

Now assumed solution Eq. (37), and its variational part Eq. (38) are substituted into Eq. (36). However, variations in δg_l^i functions are arbitrary, hence the coefficients of δg_l^i should be equal to zero individually according to fundamental lemma of variational principles. It leads to the following set of $8n$ first-order coupled ODEs and $5n$ coupled linear-algebraic equations for every layer,

$$\mathbf{M}\bar{\mathbf{G}}_{,\zeta} = \bar{\mathbf{A}}^{\mathbf{m}}(\omega)\bar{\mathbf{G}} + \hat{\mathbf{A}}^{\mathbf{m}}\hat{\mathbf{G}} \tag{40}$$

$$\mathbf{K}^{\mathbf{m}}\hat{\mathbf{G}} = \tilde{\mathbf{A}}^{\mathbf{m}}\bar{\mathbf{G}} \tag{41}$$

Here, $\mathbf{M}_{8n\times 8n}$, $\bar{\mathbf{A}}_{8n\times 8n}$, $\hat{\mathbf{A}}_{8n\times 5n}$, $\mathbf{K}_{5n\times 5n}$, and $\tilde{\mathbf{A}}_{5n\times 8n}$ are coefficient matrices, wherein $\bar{\mathbf{A}}^{\mathbf{m}} = \bar{\mathbf{A}} + \bar{\mathbf{A}}^{\mathbf{v}}$; $\hat{\mathbf{A}}^{\mathbf{m}} = \hat{\mathbf{A}} + \hat{\mathbf{A}}^{\mathbf{v}}$; $\mathbf{K}^{\mathbf{m}} = \mathbf{K} + \mathbf{K}^{\mathbf{v}}$; $\tilde{\mathbf{A}}^{\mathbf{m}} = \tilde{\mathbf{A}} + \tilde{\mathbf{A}}^{\mathbf{v}}$. The non-zero elements of coefficient matrices of Eqs. (40) and (41) ($\mathbf{M}$, $\bar{\mathbf{A}}$, $\bar{\mathbf{A}}^{\mathbf{v}}$, $\hat{\mathbf{A}}$, $\hat{\mathbf{A}}^{\mathbf{v}}$, $\mathbf{K}^{\mathbf{m}}$, $\tilde{\mathbf{A}}$, $\tilde{\mathbf{A}}^{\mathbf{v}}$) are listed in Appendix C (refer to the supplementary material). Since the functions f_l^i are presumed for first starting iteration, the coefficient elements of

Eqs. (40) and (41) could be solved in closed-form by performing integration along x-direction. Hence, coefficients of Eq. (40) and Eq. (41) are now known. The substitution of $\hat{\mathbf{G}}$ from Eq. (41) into Eq. (40), transforms Eq. (40) to the following form,

$$\bar{\mathbf{G}}_{,\zeta} = \mathbf{A}(\omega)\bar{\mathbf{G}}, \qquad \text{Here,} \qquad \mathbf{A} = \mathbf{M}^{-1}[\bar{\mathbf{A}}^{\mathbf{m}} + \hat{\mathbf{A}}^{\mathbf{m}}\mathbf{K}^{\mathbf{m}-1}\bar{\mathbf{A}}^{\mathbf{m}}] \tag{42}$$

Above Eq. (42) is a set of $8n$ first-order coupled ODEs with constant coefficients and this system of ODEs can be solved analytically by following solution approach suggested by Kumari and Behera [92] which is further explained in Appendix D (refer to the supplementary material).

4.2. Second iterative step—solving functions $f_l^i(\xi_1)$

In the first iterative step, $g_l^i(\zeta)$ functions are obtained in closed-form. Now, in the second iteration these obtained $g_l^i(\zeta)$ functions are used to obtain f_l^i functions, which are assumed as unknown in this iteration. Therefore, variation is assumed in g_l^i functions and hence $\delta\mathbf{X_l}$ can be expressed as,

$$\delta X_l(\xi_1,\zeta) = \sum_{i=1}^{n} g_l^i(\zeta)\delta f_l^i \qquad \text{for} \quad l = 1,2,\ldots,13 \tag{43}$$

Similar to first iteration, the in-plane functions $f_l^i(\xi_1)$ can also be split-up into two column vectors $\hat{\mathbf{F}}$ and $\bar{\mathbf{F}}$. Here, $\bar{\mathbf{F}}$ contains the specific independent variables that appear in the mechanical and electrical boundary conditions along x-directions at $\xi_1 = 0$ and 1. The $\hat{\mathbf{F}}$ column vector contains the remaining dependent variables. Hence,

$$\begin{aligned}\bar{\mathbf{F}} &= \left[f_1^1 \ldots f_1^n \quad f_2^1 \ldots f_2^n \quad f_3^1 \ldots f_3^n \quad f_4^1 \ldots f_4^n \quad f_7^1 \ldots f_7^n \quad f_9^1 \ldots f_9^n \quad f_{10}^1 \ldots f_{10}^n \quad f_{11}^1 \ldots f_{11}^n\right]^{\mathrm{T}} \\ \hat{\mathbf{F}} &= \left[f_5^1 \ldots f_5^n \quad f_6^1 \ldots f_6^n \quad f_8^1 \ldots f_8^n \quad f_{12}^1 \ldots f_{12}^n \quad f_{13}^1 \ldots f_{13}^n\right]^{\mathrm{T}}\end{aligned} \tag{44}$$

Substituting Eq. (43) and Eq. (37) in Eq. (36), and equating the coefficient of δf_l^i to zero individually, lead to a set of differential–algebraic equations as,

$$\mathbf{N}\bar{\mathbf{F}}_{,\xi_1} = \{\bar{\mathbf{B}}(\omega) + \xi_1\bar{\mathbf{B}}^{\mathbf{v}}(\omega)\}\bar{\mathbf{F}} + (\hat{\mathbf{B}} + \xi_1\hat{\mathbf{B}}^{\mathbf{v}})\hat{\mathbf{F}} \tag{45}$$

$$\mathbf{L}\hat{\mathbf{F}} = (\tilde{\mathbf{B}} + \xi_1\tilde{\mathbf{B}}^{\mathbf{v}})\bar{\mathbf{F}} \tag{46}$$

where $\mathbf{N}_{8n\times8n}$, $\bar{\mathbf{B}}_{8n\times8n}$, $\bar{\mathbf{B}}^{\mathbf{v}}_{8n\times8n}$, $\hat{\mathbf{B}}_{8n\times5n}$, $\hat{\mathbf{B}}^{\mathbf{v}}_{8n\times5n}$, $\mathbf{L}_{5n\times5n}$, $\tilde{\mathbf{B}}_{5n\times8n}$ and $\tilde{\mathbf{B}}^{\mathbf{v}}_{5n\times8n}$ are coefficient matrices and all non-zero elements of these matrices are listed in Appendix E (refer to the supplementary material). However, $g_l^i(\zeta)$ are already known in closed-form from previous iteration, hence all elements of the coefficient matrices can also be solved exactly in closed form by executing integration over ζ direction on the known g_l^i functions. Then, substitution of algebraic Eq. (46) into Eq. (45) leads to,

$$\bar{\mathbf{F}}_{,\xi_1} = \{\mathbf{B_0}(\omega) + \xi_1\mathbf{B_1}(\omega) + \xi_1^2\mathbf{B_2}\}\bar{\mathbf{F}} \tag{47}$$

Here $\mathbf{B_0} = \mathbf{N^{-1}}(\bar{\mathbf{B}} + \hat{\mathbf{B}}\mathbf{L^{-1}}\tilde{\mathbf{B}})$, $\mathbf{B_2} = \mathbf{N^{-1}}(\hat{\mathbf{B}}^{\mathbf{v}}\mathbf{L^{-1}}\tilde{\mathbf{B}}^{\mathbf{v}})$, $\mathbf{B_1} = \mathbf{N^{-1}}(\bar{\mathbf{B}}^{\mathbf{v}} + \hat{\mathbf{B}}\mathbf{L^{-1}}\tilde{\mathbf{B}}^{\mathbf{v}} + \hat{\mathbf{B}}^{\mathbf{v}}\mathbf{L^{-1}}\tilde{\mathbf{B}})$. The above Eq. (47) represents coupled system of first-order differential equations ($8n$) having variable coefficients which are function of ξ_1. This couple system ODEs cannot be solved exactly using traditional approaches. Therefore, solution of Eq. (47) has been obtained by utilizing a modified power series approach recently developed by Singh and Kumari et al. [40,73], which is explained in Appendix F (Supplementary material). After obtaining $\bar{\mathbf{F}}$ functions in closed-form, further they have been used to obtain the $\hat{\mathbf{F}}$ functions using Eq. (46). In this way second iterative step is completed which gives solution along in-plane (x) direction. These two iteration steps, first for thickness functions g_l^i which is explained in (Section 4.1), and second for f_l^i functions which is explained in (Section 4.2), complete one iteration. After one iteration these g_l^i and f_l^i are known and then, it has been used for obtaining final solution based on Eqs. (35) and Eq. (37). These two iterative steps can be continued to get the final converged solution depending on the required level of accuracy.

5. Numerical results and discussion

This section presents numerical results concerning validation of the proposed analytical framework first, followed by in-depth elastic and viscoelastic analyses.

5.1. Elastic analysis

5.1.1. Hybrid piezoelectric rectangular plates of constant stiffness and density

The developed mathematical model is validated first by comparing the present results with previously published results in the literature to establish and demonstrate the accuracy of the proposed analytical solution approach. In the following subsections, the effect of in-plane graded elastic properties on natural frequencies and mode shapes of intelligent FGM plates is investigated extensively. New benchmark results are presented for various gradation cases by considering different configurations and thickness ratios ($S = a/h$) under different electrical and mechanical boundary conditions. The material properties [93] used in this study are tabulated in Table 2.

Various configurations of smart plates, as shown in Fig. 3, are taken into consideration for the current numerical study. The obtained results for natural frequencies are expressed in non-dimensionalized form using $\omega^* = \omega a S\sqrt{\rho_0/Y_0}$. Where $Y_0 = 6.9$ GPa for

Table 2
Material constants [93].

Material	Y_1	Y_2	Y_3	G_{23}	G_{13}	G_{12}	ν_{12}	ν_{13}	ν_{23}	ρ
Mat. 1	6.9	6.9	6.9	1.38	1.38	1.38	0.25	0.25	0.25	1578
Mat. 2	224.25	6.9	6.9	1.38	56.58	56.58	0.25	0.25	0.25	1578
Mat. 3	172.5	6.9	6.9	1.38	3.45	3.45	0.25	0.25	0.25	1578
Mat. 4 (Gr/Ep)	181.0	10.3	10.3	2.87	7.17	7.17	0.28	0.28	0.33	1578
Mat. 5 (Face)	131.1	6.9	6.9	2.3322	3.588	3.588	0.32	0.32	0.49	1000
Mat. 6 (Core)	0.0002208	0.0002208	2.76	0.4554	0.5451	0.01656	0.99	3×10^{-5}	3×10^{-5}	70
PZT-5A	61.0	61.0	53.2	21.1	21.1	22.6	0.35	0.38	0.38	7600
Material	d_{31}	d_{32}	d_{33}	d_{24}	d_{15}	η_{11}	η_{22}	η_{33}		
PZT-5A	−171	−171	374	584	584	15.3	15.3	15.0		

Units: density (ρ) in Kg/m^3; Young's moduli Y_i in GPa and shear moduli G_{ij} in GPa; electric permittivities η_{ij} in nF/m; piezoelectric strain coefficients d_{ij} in pm/V; where $d_0 = d_{33}$ pm/V.

Table 3
Comparison of first six lowest flexural frequencies for all-around simply supported (SSSS) single-layered square smart piezoelectric plates under closed circuit (CC) condition ($\phi(x, y, \pm h/2) = 0$ and open circuit (OC) condition ($D_z(x, y, \pm h/2) = 0$).

	Closed circuit			Open circuit		
	Present	3D Analytical [92]	3D Exact [94]	Present	3D Analytical [92]	3D Exact [94]
$S = 4$	96929.9	96929.9	96929.9	98233.0	98231.7	98231.7
	194254.8	194254.8	194255.0	194254.8	194254.8	194255.0
	327662.5	327662.5	327663.0	355170.5	355110.0	355110.0
	538884.4	538884.4	538885.0	538884.4	538884.4	538885.0
	609187.1	609185.3	609186.0	690984.2	690766.8	690767.0
	958929.5	958922.4	958922.0	960118.1	960103.9	960103.0
$S = 1$	713025.6	713062.7	713061.0	724559.2	724602.0	724602.0
	777020.5	777020.5	777021.0	777020.5	777020.5	777021.0
	889887.0	889901.3	889902.0	912882.9	912911.4	912912.0
	925431.5	925431.5	925431.0	925431.5	925431.5	925431.0
	1243806.5	1243817.9	1243819.0	1270594.7	1270594.7	1270594.0
	1270594.7	1270594.7	1270594.0	1293476.5	1293505.0	1293504.0

hybrid smart plate (b) and (c), and $Y_0 = 10.3$ GPa for all other hybrid smart plates and in-plane functionally graded (IPFG) plates. Similarly, $\rho_0 = 1000$ Kg/m^3 for hybrid smart plate (c), and $\rho_0 = 1578$ Kg/m^3 for all other hybrid smart plates and inplane IPFG plates. Similarly, non-dimensionalized values of modal displacements, electrical state variables and stresses are plotted in graphical figures, and the following expression is used for the non-dimensionalization of results.

$$(\bar{w},\ \bar{v},\ \bar{u}) = (w, v, u)/\max(w, v, u); \qquad (\bar{\sigma}_i,\ \bar{\tau}_{ij}) = (\sigma_i,\ \tau_{ij})\, h\, S/(Y_0 \max(w, u))$$
$$\bar{\phi} = \phi\, d_0/\max(w, u) \qquad \bar{D}_i = D_i\, h\, S/(d_0\ Y_0 \max(w, u))$$

$\bar{w}$, $\bar{v}$, $\bar{u}$ denotes the non-dimensionalized displacement in z, y, and x directions. Normalized normal stresses and shear stresses are denoted by $\bar{\sigma}_i$ and $\bar{\tau}_{ij}$, respectively. Similarly, $\bar{\phi}$ expresses non-dimensionalized electric potential, and normalized electric displacements are expressed by $\bar{D}_i$. Here $S(= a/h)$ expresses the span-to-thickness ratio of FGM plate and $\max(w, v, u)$ denotes the largest value of displacement w, v and u along the thickness of FGM plate for that flexural mode. The length of all FGM and composite plates are taken equal to unity ($a = 1$) for all cases and thickness of rectangular plate is assumed according to span to thickness ratio ($S = a/h$) of the plates. For $S = 5, 10, 20$ the values of h are 0.2, 0.1, 0.05, respectively. Similarly, $s(= h/a)$ expresses the thickness-to-span ratio. The rectangular plates are named corresponding to their mechanical support conditions at the ends. For example, CFSS designation of plate indicates that plate is clamped (C) at $\xi_1 = 0$ and free (F) at $\xi_1 = 1$, and simply-supported at $\xi_2 = 0$ and $\xi_2 = 1$.

Here the present EKM-Fourier series technique of solution is validated by comparing the results with previously reported numerical results for constant property cases without any type of gradation. First, the present results are validated for an orthotropic single-layered piezoelectric rectangular plate subjected to a simply-supported boundary condition and it has poling [Remark 2: Appendix G (supplementary material)] along the z-direction. Results are compared with the 3D exact result of Heyliger and Saravanos [94], which was obtained by employing the Fourier series approach through which the solution of the ordinary differential equations can be obtained in the exact closed form (therefore, referred as the exact solution approach in literature), and 3D elasticity-based analytical results of Susanata and Kumari [92]. In Table 3, the results are compared for two-type of electrical arrangements, (i) Single-layered PZT-5 A plate subjected to closed-circuit (CC) condition at top and bottom surface ($\phi(x, y, \pm h/2) = 0$), (ii) Single-layered PZT-5 A plate subjected to Open-circuit (OC) condition at top and bottom surface ($D_z(x, y, \pm h/2) = 0$). Results are compared for thick plates having thickness ratio $S = 4$ and $S = 1$ (Cubical-plate). It is noted that the current power series-based EKM solution is accurate in predicting natural frequencies of single-layered smart piezoelectric plate, and all results are in good agreement.

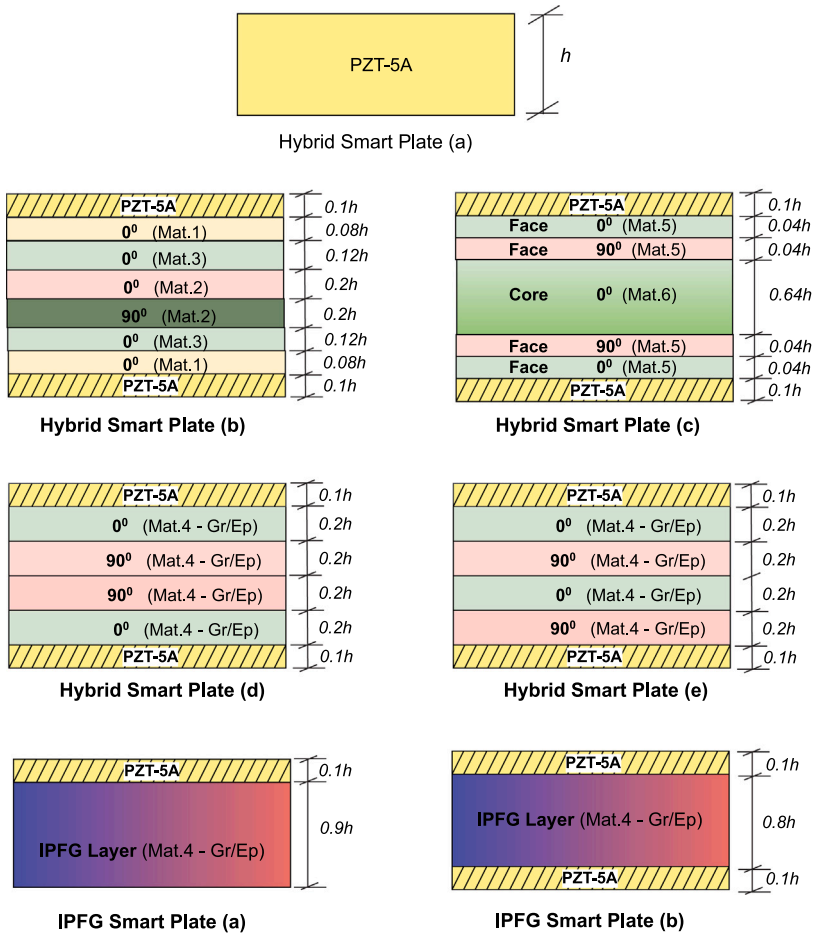

Fig. 3. Configurations of smart IPFG rectangular plates considered for the present numerical study.

Table 4
Comparison of natural frequencies ($\omega^* = \omega a S\sqrt{\rho_0/Y_0}$) of hybrid smart plate (b), intelligent sandwich plate (c), composite smart plate (d) and (e) with different S values and electrical condition as $\phi(x, y, -h/2) = 0$ and $D_z(x, y, h/2) = 0$.

		Smart plate (b)		Smart plate (c)		Smart plate (d)		Smart plate (e)	
	S	Present	3D Exact [93]	Present	3D Exact [93]	Present	3D Exact [93]	Present	3D Exact [93]
ω^*_{11}	5	7.4148	7.4148	4.5233	4.5277	7.1810	7.1810	7.1809	7.1809
	10	10.0342	10.0342	7.3390	7.3390	9.3686	9.3686	9.2795	9.2795
	20	11.4178	11.4178	9.7440	9.7440	10.4327	10.4327	10.2231	10.2231
ω^*_{21}	5	14.7140	14.7140	7.8958	7.8958	13.5944	13.5944	13.6391	13.6391
	10	22.3965	22.3965	13.8801	13.8801	21.2357	21.2357	20.4789	20.4779
	20	29.0240	29.0240	21.3567	21.3567	27.8333	27.8333	25.2664	25.2664
ω^*_{31}	5	23.6208	23.6208	11.9501	11.9501	20.9313	20.9313	21.0482	21.0482
	10	37.7411	37.7411	21.2309	21.2357	35.0186	35.0186	34.5431	34.5431
	20	53.5800	53.5800	35.6934	35.6934	51.6591	51.6591	47.5942	47.5942
ω^*_{22}	5	18.6431	18.6431	10.2915	10.2915	18.3672	18.3672	18.2319	18.2319
	10	29.6593	29.6593	18.0932	18.0103	28.7240	28.7240	28.7234	28.7234
	20	40.1367	40.1367	29.3559	29.3559	37.4744	37.4744	37.1180	37.1180
ω^*_{33}	5	30.7853	30.7853	16.9820	16.9820	29.7901	29.7901	29.4727	29.4727
	10	51.5468	51.5468	29.2571	29.2571	50.7313	50.7313	50.5764	50.5764
	20	77.4823	77.4823	50.7073	50.7073	73.8647	73.8647	73.6951	73.6951

After establishing the accuracy of the present mathematical model for single-layered piezoelectric smart plate (a), the results are obtained for laminated piezoelectric plates (b), (c), (d), and (e) of different configurations, as shown in Fig. 3. All the laminated hybrid plates are integrated with two PZT-5 A plies at the bottom and top to their elastic substrate. The thickness of both top

and bottom piezoelectric layers is $0.1h$ and it has poling along with the thickness (z-direction). The surfaces of piezoelectric layers with the elastic substrate are considered grounded ($\phi = 0$). The elastic substrate of plate (b) has six laminae with orientation θ_k as $[0^\circ/0^\circ/90^\circ/0^\circ/0^\circ/0^\circ]$ with thickness $0.08h/0.12h/0.2h/\ 0.2h/0.12h/0.08h$ of material 1/3/2/2/3/1, as shown in Fig. 3. The elastic substrate of the plate (c) is a five-layer sandwich substrate with two faces $[0^\circ/90^\circ]$ of Material 5 and a soft-core $[0^\circ]$ of Material 6. Overall orientation of substrate is $[0^\circ/90^\circ/0^\circ/90^\circ/0^\circ]$ of thicknesses $0.04h/0.04h/0.64h/0.04h/0.04h$ and material 5/5/6/5/5, as shown in Fig. 3. The elastic substrate of the plate (d) and (e) has a 4-ply composite laminate of graphite-epoxy Mat.4, and each ply is of equal thickness $0.2h$. Plate (d) has symmetric substrate with lay-up $[0^\circ/90^\circ/90^\circ/0^\circ]$ and the of plate (e) has antisymmetric substrate with lay-up $[90^\circ/0^\circ/90^\circ/0^\circ]$, as shown in Fig. 3. The all above mentioned stacking sequences are from the base layer to top layer for all plates, as shown in Fig. 3. The dimensionless flexural frequencies are tabulated in Table 4 for plates (b), (c), (d) and (e) with the upper surface grounded ($\phi(x, y, h/2) = 0$) and the bottommost surface subjected to open-circuit conditions ($D_z(x, y, \pm -h/2) = 0$. The flexural frequencies are listed for different span to thickness ratio, S = 5,10, 20, and for different mode, (m, n) = (1, 1), (2, 1), (2, 2), (3, 1), (3, 3). The present numerical results for hybrid smart plates (b), (c), (d) and (e) are compared with the 3D exact results presented by Kapuria and Achary [93], which is also based on the Fourier series approach, known as an exact solution. It is noted that the current power-series EKM model is very much accurate in predicting flexural frequencies for symmetric and antisymmetric laminated/sandwich piezoelectric smart plates. All numerical results are in excellent agreement with the 3D exact results of [93]. The current model is highly efficient and accurate, and moreover, accuracy is not affected much by thickness to span ratio S and inhomogeneity in configurations.

After demonstrating the validation for simply-supported smart piezoelectric plates, the validation is carried out for piezo-laminated smart rectangular plates subjected to arbitrary support conditions. The numerical results obtained from the present power series-based EKM model are compared with the result presented by Susanta and Kumari [92] which are obtained using 3D exact EKM. Table S1 (in the supplementary material) shows the comparison of the first ten lowest natural bending frequencies for thick (S = 5) and moderately thick (S = 10) hybrid smart plates (d) under different mechanical support conditions such as SSSS, CSSS, CCSS, CFSS, and FFSS. Excellent agreement is observed for all the cases. It demonstrates that the present power-series approach is efficient, yet accurate in solving coupled system of ODEs for dynamic cases. It is worth noting that one term (n = 1) based EKM solution is enough to predict the natural frequencies of the piezoelectric plate accurately. It is also worth mentioning that the present power series-based EKM solution is equally accurate for predicting the natural frequencies of the thick and thin hybrid piezoelectric plates subjected to open or closed-circuit conditions. The effects of electrical circuit conditions are very less on flexural frequencies of the plate due to weak electro-mechanical coupling, but these tiny effects play a vital role in precise control and sensory applications. It is observed that the present mathematical model is very accurate and precise in predicting these small effects, as illustrated in Table 3, 4 and S1 (Supplementary material).

5.1.2. Hybrid piezoelectric rectangular plates with variable stiffness and density

After demonstrating the accuracy and efficacy of the current 3D mathematical model for constant stiffness piezoelectric plates, the numerical study is extended to the analysis of functionally graded smart piezo-plates in this section. Two types of smart FGM plates are taken into consideration for the numerical study, (i) IPFG Plate (a): In-plane functionally graded rectangular substrate integrated with a single piezoelectric layer at the top; and (ii) IPFG Plate (b): In-plane functionally graded rectangular substrate integrated with the piezoelectric layer at bottom and top, as shown in Fig. 3. The thickness of PZT-5 A layers is 0.1 h for both type of IPFG plates. To study the effect of in-plane stiffness variation on dynamic behaviour of smart plates, three types of stiffness and density gradation cases are considered for the elastic layers, Case (1): $\delta_1 = \delta_2 = \delta_p = 0.5$; Case (2): $\delta_1 = \delta_2 = \delta_p = 1.0$; and Case (3): $\delta_1 = 2.0$, $\delta_2 = 1.0$, $\delta_p = 1.5$ along with homogenous plate (constant properties) case (Constant: $\delta_1 = \delta_2 = \delta_p = 0.0$). The numerical results for homogenous (constant) property case are also presented along with graded density and stiffness cases to access the influence of in-plane variation of stiffness and density on the flexural frequencies and electro-mechanical behaviour of IPFG plates. Only converged results are tabulated here, which are obtained by taking n = 1, iter.1 for SSSS smart plate and n = 1, iter.2 for all other types of support conditions. The convergence study of the present EKM approach is presented in Table S2 (supplementary material). In subsequent sections, three-dimensional finite element (3D FE) results, obtained using commercial finite element analysis (FEA) software ABAQUS, are also listed along with present EKM results for validation purposes because no other analytical and semi-analytical solution exists in literature for free-vibration of variable-stiffness piezoelectric plates. For 3D FE analysis, user material subroutine (UMAT) is developed to implement the in-plane gradation of stiffness and density in the finite element model and then converged FE results are obtained by using a discretization of 50 (length) × 50 (width) × 18 (thickness). For comparison and bench-marking purposes, the numerical results are tabulated for various type of electrical and mechanical supports under different thickness ratios.

5.1.2.1. IPFG plate (a): In-plane functionally graded rectangular elastic substrate integrated with piezoelectric layer at top. An in-plane functionally graded plate (a) integrated with a smart piezoelectric (PZT-5 A) layer of thickness 0.1 h at the top, as shown in Fig. 3, is taken into consideration for numerical study in this section. The stiffness and density of the elastic composite layer are assumed to vary linearly along the axial (x) direction where the elastic and electrical properties of the piezoelectric layer are assumed constant. The side edges and top/bottom surface of the active piezoelectric layer are considered under close-circuit conditions. First five lowest dimensionless fundamental flexural frequencies ($\omega^* = \omega a S\sqrt{\rho_0/E_0}$, here E_0 = 10.3 GPa, ρ = 1578 kg/m^3) are tabulated for m = 1, 2 and 3 considering moderately thick (S = 10) hybrid plate (a) under different mechanical support conditions. Results are listed for three gradation cases, *i.e.* Case (1), Case (2), and Case (3), along with homogeneous plate (constant properties case) to investigate the influence of in-plane variation of stiffness and density gradation on flexural frequencies. Tables 5 and 6 contain benchmark

Table 5
Influence of in-plane gradation of density and stiffness on natural flexural frequencies ($\omega^* = \omega a S\sqrt{\rho_0/E_0}$) of moderately thick ($S = 10$) IPFG smart piezoelectric plate (a) subjected to CCSS boundary conditions.

	Constant		Case (1)		Case (2)		Case (3)	
ω^*_{nm}	Present	3D FE	Present	3D FE	Present	3D FE	Present	3D FE
ω^*_{11}	15.390	15.489	12.978	13.099	10.422	11.403	10.095	10.350
ω^*_{21}	32.424	32.719	27.264	27.542	23.591	23.878	21.609	21.893
ω^*_{31}	52.017	52.585	43.763	44.260	37.874	38.348	34.936	35.382
ω^*_{41}	72.422	73.239	61.041	61.726	52.846	53.473	49.052	49.639
ω^*_{51}	93.019	94.057	78.703	79.483	68.166	68.903	63.588	64.264
ω^*_{12}	20.029	20.023	17.665	17.506	15.970	15.662	14.164	14.509
ω^*_{22}	35.752	36.000	30.489	30.724	26.716	26.962	24.711	24.960
ω^*_{32}	54.645	55.158	46.296	46.747	39.490	40.746	37.382	37.790
ω^*_{42}	74.610	75.381	63.149	63.795	54.871	55.465	51.079	51.638
ω^*_{52}	95.377	95.847	80.406	81.241	69.845	70.600	65.259	65.964
ω^*_{13}	29.065	29.224	26.133	26.275	23.841	23.977	22.276	22.407
ω^*_{23}	42.431	42.632	37.002	37.192	33.040	33.245	30.848	31.059
ω^*_{33}	59.759	60.187	51.322	51.697	45.232	45.596	42.201	42.549
ω^*_{43}	78.119	79.416	67.225	67.796	58.623	59.397	55.013	55.509
ω^*_{53}	98.246	99.174	83.813	84.573	73.198	73.890	68.556	69.203

Table 6
Effect of in-plane gradation (density and stiffness) on natural flexural frequencies ($\omega^* = \omega a S\sqrt{\rho_0/E_0}$) of moderately thick ($S = 10$) IPFG piezoelectric plate (a) for CFSS boundary condition.

	Constant		Case (1)		Case (2)		Case (3)	
ω^*_{nm}	Present	3D FE	Present	3D FE	Present	3D FE	Present	3D FE
ω^*_{11}	5.199	5.226	4.489	4.507	3.984	3.996	3.628	3.636
ω^*_{21}	17.306	17.377	14.866	14.923	13.066	13.123	11.704	11.771
ω^*_{31}	36.543	36.966	31.267	31.051	27.376	27.375	24.764	24.805
ω^*_{41}	57.271	57.494	48.841	48.985	42.615	42.763	39.103	39.256
ω^*_{51}	78.411	79.372	66.622	67.341	58.109	58.554	53.830	54.201
ω^*_{12}	12.914	13.029	11.399	11.515	10.301	10.403	9.511	9.597
ω^*_{22}	22.869	22.936	20.014	20.070	17.911	17.963	16.487	16.547
ω^*_{32}	40.273	40.530	34.747	34.910	30.670	30.801	28.111	28.243
ω^*_{42}	60.118	60.462	51.512	51.754	45.147	45.352	41.665	41.872
ω^*_{52}	80.222	80.476	68.800	69.392	60.139	60.617	55.880	56.282
ω^*_{13}	24.382	24.537	21.685	21.830	19.712	19.790	18.148	18.263
ω^*_{23}	32.236	32.333	28.777	28.860	26.182	26.256	24.423	24.500
ω^*_{33}	47.100	47.317	41.240	41.383	36.893	37.008	34.248	34.362
ω^*_{43}	65.348	65.809	56.543	56.813	50.004	50.202	46.476	46.658
ω^*_{53}	84.524	85.722	72.866	73.438	64.089	64.454	59.784	60.086

results for CCSS and CFSS support conditions, respectively. Subsequently, the results are for SSSS, CSSS, SFSS, and FFSS support conditions are tabulated in Table S3, S4, S5 and S6 (refer to the supplementary material), respectively. The fundamental flexural frequencies for the in-plane graded hybrid plate are presented for the first time in this paper. As the gradation index for elastic properties and density increases, the natural frequencies decrease remarkably under all the support conditions. The quantitative effect of in-plane variation of density and stiffness on flexural frequencies of hybrid rectangular plate primarily depends on the mechanical support conditions of the IPFG plate. Percentage decrement in flexural frequencies due to the in-plane variation of properties are plotted in Figs. S1, S2 and S3 of the supplementary material. An interesting observation is that the extent of the effect of gradation on lower natural frequencies for $m = 1$, 2, and 3 significantly depends upon the type of support conditions. On the other hand, the influence of gradation on higher mode natural flexural frequencies (for $m = 1$, 2, and 3) shows independence from mechanical support conditions. The percentage change in higher mode natural flexural frequencies is nearly the same for all support conditions. This observation is physically relevant considering the fact that higher flexural vibration modes are more local in nature. For all hybrid plated, except FFSS plate, nearly 10 to 15% decrement is noted in the lowest five flexural frequencies ($m = 1$,2, and 3) for Case (1) compared to the constant property case. For Case (2) and Case (3), the percentage decrease in flexural frequencies are 16 to 27% and 22 to 34% for Case (3), respectively. For the FFSS hybrid plate, these decrements are 7%–14% for Case (1), 12%–26% for Case (2), and 15%–33% for Case (2). All results reported in this section have been computed by taking $n = 1$, iteration 1 for SSSS support conditions and $n = 1$, iteration 2 for other support conditions.

After studying the influence of in-plane gradation of stiffness and density on the natural flexural frequencies of the hybrid smart plate, the numerical investigation is extended to access the impact of in-plane gradation on mode shapes of the hybrid plate. The flexural 3D mode shapes associated with the lowest five natural frequencies are plotted for different types of support conditions under constant properties case and gradation Case 1. The 3D mode shapes for the SSSS hybrid IPFG plate are displayed for constant property case and gradation Case 1 in Figs. S4 and S5, respectively. Similarly, the 3D mode shapes for the CSSS hybrid IPFG plate

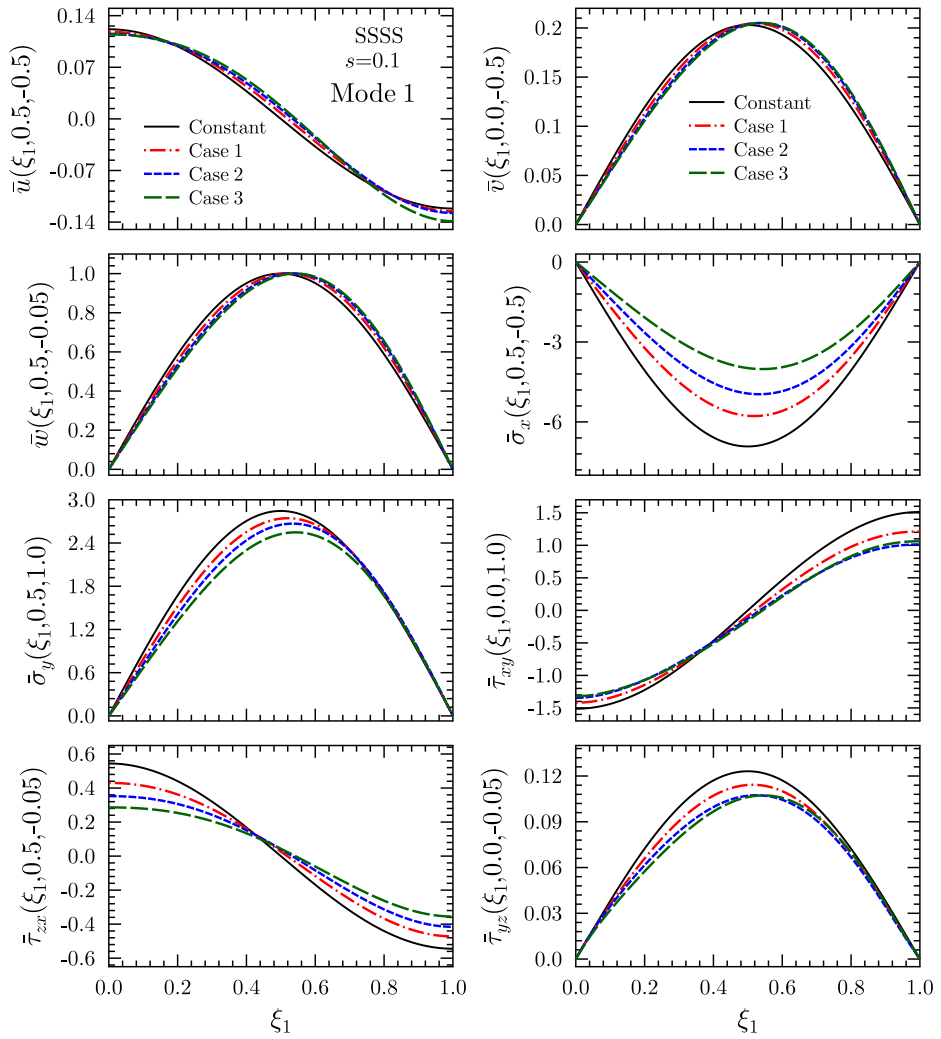

Fig. 4. Influence of in-plane variation of density and stiffness on axial variations of displacements and stresses for first flexural vibration mode (Mode-1) of the moderately thick (S = 10) IPFG smart plate (a) subjected to SSSS boundary condition.

are displayed for homogenous case (constant property case) and gradation Case 1 in Figs. S6 and S7. Figs. S8 and S9 contain 3D mode shapes for the CCSS hybrid IPFG plate for constant property case and gradation case 1, respectively. Similarly, the 3D mode shapes for other boundary conditions are also plotted to investigate the influence of gradation in detail. In Figs. S10 and S11 results are plotted for CFSS plates. Mode shapes of SFSS and FFSS hybrid plates are given in Figs. S12, S13, S14 and S15 for constant property case and gradation Case (1). The Figs. S6–S15 are given in supplementary material. It is worth mentioning that all flexural mode shapes are impacted significantly by the in-plane gradation of stiffness and density. Another interesting observation is that the mode shape of the FFSS plate is affected more as compared to other support conditions.

Further, the influence of axial gradation of stiffness and density is also investigated on the longitudinal variation of flexural deflection ($\bar{w}$, $\bar{v}$, $\bar{u}$) and stresses ($\bar{\sigma}_x$, $\bar{\sigma}_y$, $\bar{\tau}_{xy}$, $\bar{\tau}_{yz}$, $\bar{\tau}_{xz}$) in the hybrid FGM plate. In Figs. 4 and 5 longitudinal variation of stresses and displacements are plotted for the first flexural vibration mode of moderately thick (S = 10) smart hybrid plate (a) subjected to SSSS and CFSS support conditions, respectively. Subsequently, the longitudinal variation of stresses and displacements are also plotted for CSSS, CCSS, and SFSS hybrid FGM plate in Figs. S16, S17, and S18 (supplementary material), respectively. In these figures, the results are plotted for all gradation cases along with the constant property case. It is found that the longitudinal variation of stresses in smart FGM plates is impacted significantly due to in-plane gradation, whereas displacement of the IPFG plates is least affected. The effect on stresses $\bar{\sigma}_x$, $\bar{\tau}_{xy}$, and $\bar{\tau}_{xz}$ are more as compared to other stresses. It is worth mentioning that the extent of the effect of gradation on displacement and stresses majorally depends on mechanical support conditions of the hybrid plate. An interesting observation is that the intelligent IPFG plate is more sensitive to the in-plane variation of density and elastic properties when subject to free edge boundary conditions such as CFSS and SFSS plates. The relative influence of gradation is most when the IPFG plates are subjected to the free-free boundary conditions. The effect is least when the hybrid piezoelectric plate is subjected to clamped

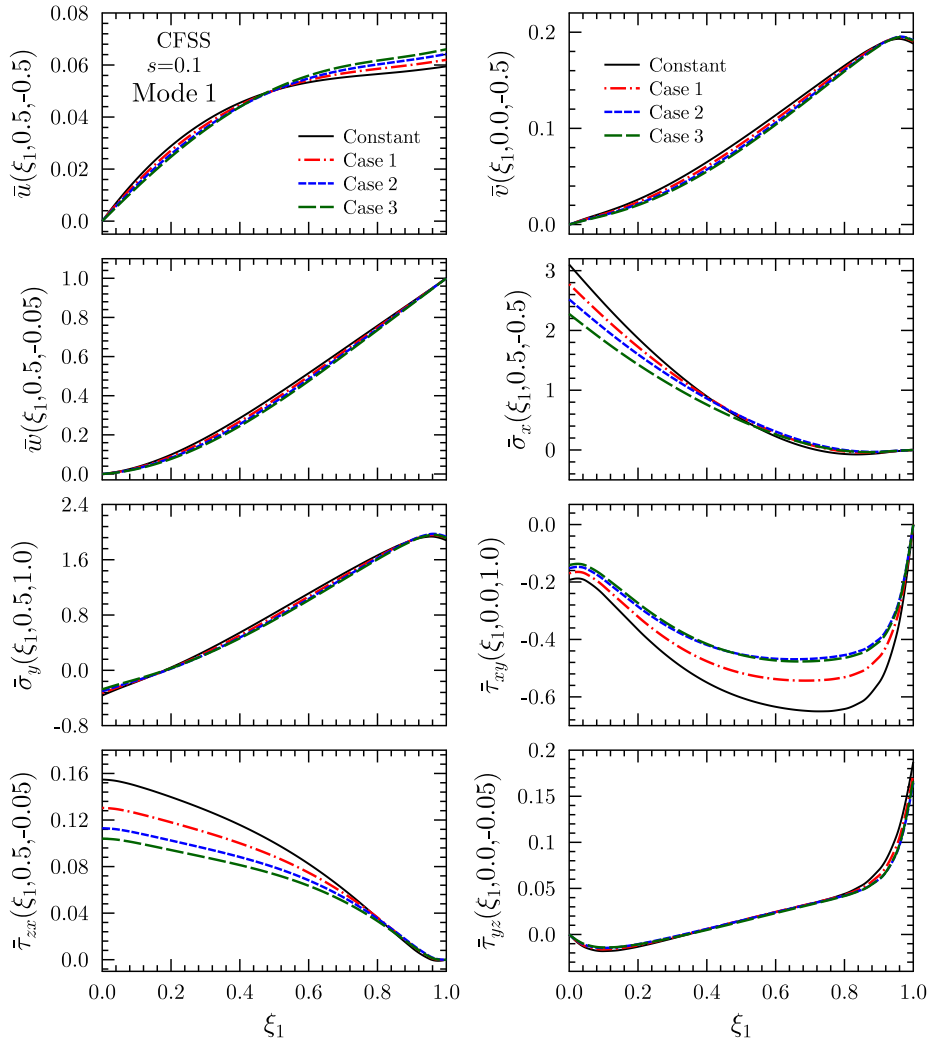

Fig. 5. Influence of in-plane variation of density and stiffness on axial variations of displacements and stresses for first flexural vibration mode (Mode-1) of the moderately thick (S = 10) IPFG smart plate (a) subjected to CFSS boundary condition.

boundary conditions. It reveals that the natural flexural vibration behaviour of the plate under in-plane gradation mainly depends upon the mechanical end conditions of the plate.

Further, to access the effect of in-plane gradation of stiffness and density on sensory behaviour of piezoelectric layers, the longitudinal variation of the electric variable ($\bar{D}_x$, $\bar{D}_y$, $\bar{D}_z$ and ϕ) are plotted for SSSS and CFSS hybrid smart plate in Figs. 6 and 7, respectively. Similarly results are also plotted for CSSS and SFSS hybrid smart plate in Figs. S19 and S20, respectively (supplementary material). It is found that the variation of electrical variables in the piezoelectric sensor layer is not affected much by longitudinal gradation of material properties in the elastic composite layers. A small effect of in-plane variation of density and stiffness is observed on electric field $\bar{D}_z$ and electric potential (ϕ) under SSSS and CSSS support conditions. It is worth noting that the natural flexural frequencies and their corresponding mode shapes are affected remarkably by the axial gradation of properties in the elastic layer, whereas the response of the sensory layer remains almost identical or affected by a very small amount. This interesting observation of the present study can play a significant role in the design of piezoelectric sensors and actuators for vibration control applications.

5.1.2.2. IPFG plate (b): In-plane functionally graded rectangular elastic substrate integrated with two piezoelectric layers at top and bottom. In this section, the longitudinal graded rectangular plate (b) which is integrated with the piezoelectric layers (PZT-5 A) at the bottom and top, as shown in Fig. 3, is investigated. The stiffness and density of the composite elastic layer are considered to vary continuously and linearly along the x-direction, whereas the material properties of the PZT layers are assumed constant. The side edges of the smart PZT-5 A layers are grounded ($\phi(y,z) = 0$ at $x = 0, a$). In Table 7 lowest ten natural flexural frequencies ($\omega^* = \omega h\sqrt{\rho_0/E_0}$, where ρ = 1578 kg/m^3, E_0 = 10.3 GPa) are presented for moderately thick (S = 10) hybrid IPFG plate (b) subjected to various mechanical edge conditions such as SSSS, CSSS, CCSS, CFSS, SFSS and FFSS. Subsequently, the results for

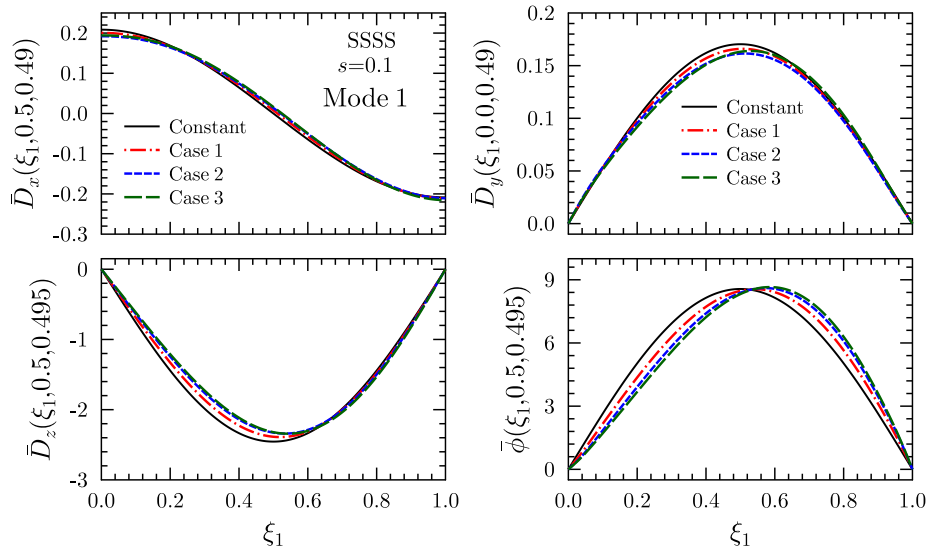

Fig. 6. Influence of in-plane variation of density and stiffness on axial variations of electric variables for first flexural vibration mode (Mode-1) of the moderately thick (S = 10) IPFG smart plate (a) subjected to SSSS boundary condition.

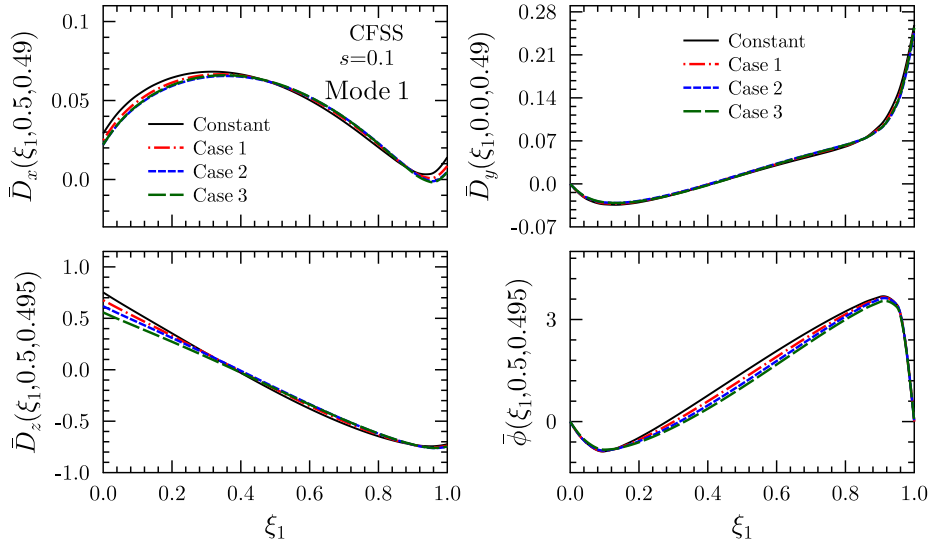

Fig. 7. Influence of in-plane variation of density and stiffness on axial variations of electric variables for first flexural vibration mode (Mode-1) of the moderately thick (S = 10) IPFG smart plate (a) with CFSS boundary condition.

thick (S = 5) hybrid IPFG plate (b) are tabulated in Table S7 (refer to the supplementary material), respectively. The benchmark numerical results are tabulated for three gradation cases (Case 1, Case 2, Case 3) along with the homogeneous (constant property) case. Significant effect of in-plane variation of density and stiffness is noted on the natural flexural frequencies of IPFG plates. The natural flexural frequencies show significant decrement as the gradation index increases. The extent of the gradation influence mainly relies on mechanical edge conditions of the hybrid IPFG plate.

Further, to assess the effect of in-plane gradation of stiffness and density on sensory behaviour of piezoelectric layers, the longitudinal variation of the electric variable ($\bar{D}_x$, $\bar{D}_y$, $\bar{D}_z$ and ϕ) are plotted for SSSS, CSSS and SFSS hybrid smart IPFG plate (b) in Figs. S21, S22 and S23, respectively (supplementary material). It is found that the variation of electrical fields ($\bar{D}_x$, $\bar{D}_y$, $\bar{D}_z$) and potential (ϕ) in the piezoelectric sensor layer is not affected much by longitudinal gradation of material properties in the elastic composite layers. It is worth noting that the natural flexural frequencies are affected remarkably by such axial gradation, whereas the electrical response of the piezoelectric layers remains almost unaffected irrespective of configuration. This would have favourable design implications concerning sensor placements for vibration control and health monitoring applications.

Table 7
Influence of in-plane gradation of density and stiffness on lowest ten natural flexural frequencies ($\omega^* = \omega a S\sqrt{\rho_0/E_0}$) of moderately thick ($S = 10$, $t_p = 0.1$ h) IPFG smart plate (b) subjected to open–circuit conditions at top and closed-circuit bottom surface.

		1	2	3	4	5	6	7	8	9	10
		ω^*_{11}	ω^*_{12}	ω^*_{21}	ω^*_{13}	ω^*_{22}	ω^*_{23}	ω^*_{14}	ω^*_{31}	ω^*_{32}	ω^*_{24}
SSSS	Constant	9.673	18.145	24.673	29.816	30.493	39.573	42.621	42.815	47.909	50.502
	Case 1	8.715	16.869	21.633	27.971	27.381	36.243	40.093	37.233	41.514	46.816
	Case 2	7.951	15.791	19.322	26.353	24.968	33.602	37.797	33.030	37.283	43.834
	Case 3	7.288	14.935	17.706	25.051	23.410	31.896	35.909	30.727	35.045	41.824
		ω^*_{11}	ω^*_{12}	ω^*_{21}	ω^*_{13}	ω^*_{22}	ω^*_{23}	ω^*_{14}	ω^*_{31}	ω^*_{32}	ω^*_{24}
CSSS	Constant	11.613	19.029	26.603	30.229	31.850	40.448	42.845	44.059	48.109	51.073
	Case 1	10.392	17.564	23.430	28.250	28.593	36.983	40.214	38.526	42.550	47.266
	Case 2	9.419	16.345	20.983	26.542	26.041	34.213	37.861	34.321	38.292	44.171
	Case 3	8.649	15.423	19.358	25.201	24.441	32.456	35.952	32.054	36.055	42.108
		ω^*_{11}	ω^*_{12}	ω^*_{21}	ω^*_{13}	ω^*_{22}	ω^*_{23}	ω^*_{14}	ω^*_{31}	ω^*_{32}	ω^*_{24}
CCSS	Constant	13.747	20.063	28.338	30.229	33.152	40.448	43.094	45.232	49.083	51.655
	Case 1	12.083	18.350	24.608	28.250	29.419	36.983	40.417	39.218	43.092	47.584
	Case 2	10.809	16.958	21.840	26.542	26.599	34.213	38.019	34.777	38.626	44.347
	Case 3	9.999	16.040	20.341	25.201	25.068	32.456	36.128	32.613	36.464	42.301
		ω^*_{11}	ω^*_{12}	ω^*_{21}	ω^*_{22}	ω^*_{13}	ω^*_{31}	ω^*_{23}	ω^*_{32}	ω^*_{13}	ω^*_{33}
CFSS	Constant	5.369	14.536	15.533	22.666	26.832	31.731	33.179	36.870	40.118	45.047
	Case 1	4.873	13.340	13.948	20.792	24.677	28.186	30.840	33.213	36.904	41.151
	Case 2	4.480	12.380	12.682	19.265	22.922	25.408	28.904	30.310	34.257	38.014
	Case 3	4.194	11.631	11.665	18.149	21.514	23.499	27.461	28.456	32.122	36.050
		ω^*_{11}	ω^*_{21}	ω^*_{12}	ω^*_{22}	ω^*_{13}	ω^*_{31}	ω^*_{23}	ω^*_{32}	ω^*_{14}	ω^*_{33}
SFSS	Constant	4.684	13.549	14.353	21.532	26.762	29.949	32.558	35.615	40.083	44.207
	Case 1	4.294	12.181	13.212	19.841	24.642	26.467	30.361	32.033	36.894	40.386
	Case 2	3.982	11.098	12.287	18.463	22.904	23.779	28.542	29.223	34.253	37.341
	Case 3	3.749	10.168	11.552	17.417	21.502	21.882	27.152	27.405	32.120	35.420
		ω^*_{11}	ω^*_{21}	ω^*_{12}	ω^*_{22}	ω^*_{31}	ω^*_{32}	ω^*_{13}	ω^*_{23}	ω^*_{41}	ω^*_{33}
FFSS	Constant	3.866	6.377	13.568	16.031	18.075	25.773	26.102	28.103	35.343	36.248
	Case 1	3.657	5.991	12.795	15.180	16.182	23.643	24.464	26.820	31.090	33.683
	Case 2	3.471	5.680	12.049	14.553	14.739	21.956	22.841	25.931	27.863	31.630
	Case 3	3.310	5.480	11.389	14.111	13.541	20.763	21.468	25.187	25.850	30.253

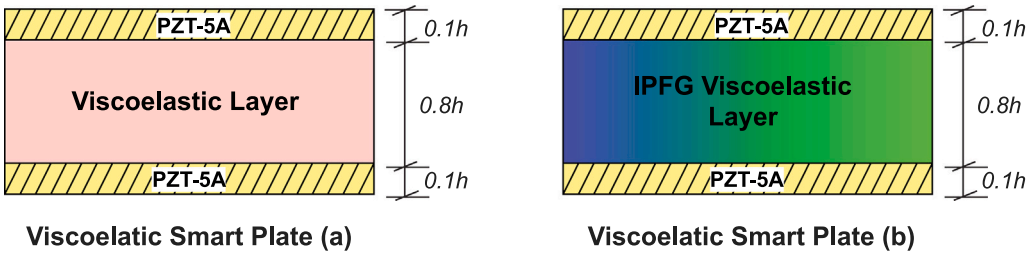

Fig. 8. Geometry of the smart in-plane functionally graded (IPFG) viscoelastic plates.

To study the effect of electrical edge conditions on the behaviour of the hybrid plate with in-plane gradation, thick ($S = 5$) hybrid plate (b) is investigated in Table S7 (supplementary material) for closed-closed circuit condition ($\phi(x, y, \pm h/2) = 0$), and closed-open circuit condition (($\phi(x, y, -h/2) = 0$ and $D_z(x, y, h/2) = 0$). The lowest six dimensionless natural flexural frequencies are listed in Table S5 for smart IPFG plate (b) under open-circuit condition at the topmost surface and closed-circuit condition at the bottommost surface. The benchmarks numerical results are listed for different types of hybrid plate boundary conditions such as SSSS, CSSS, CCSS, CFSS, SFSS, and FFSS. It is noticed that the influence of gradation on natural flexural frequencies is unchanged by the type of electric circuit conditions at the bottom and top surface of the plate. Under both types of electrical arrangements, the hybrid plate shows a similar decrement in flexural frequencies due to the in-plane variation. However, the natural frequencies of hybrid FGM plate under open-circuit conditions are slightly higher than plate subjected to closed-closed circuit conditions. It shows that the effect of electrical circuit condition is very week for the FGM hybrid plates. It is observed that the present power series-based EKM methodology can accurately determine these small effects for smart hybrid IPFG plates, which is important for precise control applications. Moreover, It is worth mentioning that these numerical results can act as benchmark to develop accurate numerical solutions for natural frequency based applications of hybrid IPFG plates. Note that the results for mode shapes, displacements, stress and strain components for various vibration modes can be readily obtained using the proposed framework, as presented in the preceding sub-section.

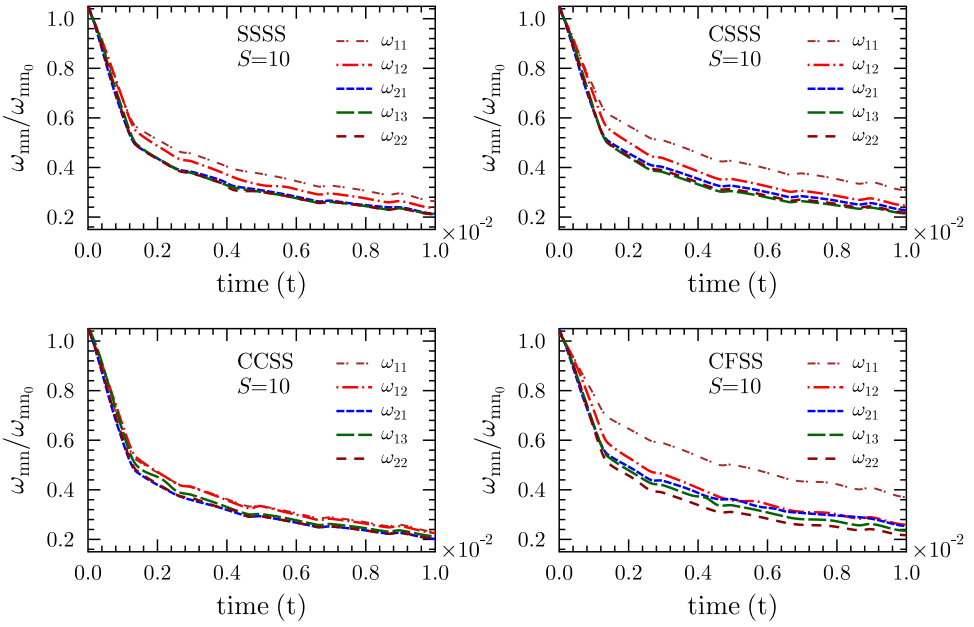

Fig. 9. Effect of viscoelasticity on the first five lowest natural frequencies of three-layered moderately thick ($S = 10$) viscoelastic smart plate (a) without graded properties. The time-dependent variation of first five lowest natural frequencies is plotted in non-dimensionalized form for different boundary conditions such as SSSS, CSSS, CCSS, CFSS. The non-dimensionalization is performed by dividing the natural frequencies of viscoelastic plate by the corresponding natural frequency of elastic plate given in Table 7.

5.2. Viscoelastic analysis of smart hybrid IPFG plates

After performing the extensive elastic analysis, the present EKM based mathematical model has been extended for viscoelastic analysis of in-plane functionally graded (IPFG) smart viscoelastic plates. The effect of viscoelasticity on the dynamic behaviours of rectangular IPFG plate is studied in detail. For that two types of configurations are considered as shown in Fig. 8.

In the viscoelastic analysis, the modulus amplitudes indicate the strength of the frequency (ω_s) domain signal, whereas the phase angle (ϕ_s) of the signal shows the alignment of frequency components in time. The variation of viscoelastic moduli amplitude and phase angle (ϕ_s) with respect to frequency are plotted in Fig. S24 (supplementary material). The variation is plotted by considering viscoelastic parameters as $\mu = (\omega_s)_{max}/1.4$ and $\epsilon = 0.2$ for obtaining the numerical results. The amplitude of elastic and shear moduli increases as the frequency (ω_s) increases until its limiting values as defined in Appendix B (supplementary material). The value of all three elastic and shear moduli at very low frequency (i.e., $\omega_s \to 0$) are equal to the classical elastic and shear moduli of elastic case. A similar trend of viscoelastic material properties is also observed for irregular honeycombs in frequency domain by Mukhopadhyay et al. [74] and for strand-based composite materials in the time domain by Malekmohammadi et al. [95]. The variation of phase angle (ϕ_s) corresponding to all three elastic and shear moduli in frequency (ω_s) domain is also plotted in Fig. S18 (Supplementary material). The phase angle achieves the peak value for a certain critical frequency, which can be calculated easily using Eq. (29). This variation of phase angle (ϕ_s) is explained by the Biot model which is similar to the linear standard viscoelastic model given in Fig. 2. In the Biot model, material behaviour is pure elastic at very low and very high frequencies, and the viscous effect is maximum at certain critical frequencies (ω_s). The phase angles (ϕ_s) variation corresponding to Young's moduli and shear moduli are same for all cases, unlike the amplitude of elastic and shear moduli. It is worth noting that the phase angles are not dependent on the material's elastic properties and their values corresponding to different Young's moduli and shear modulus remain unchanged, unlike amplitude of elastic and shear moduli.

After obtaining the variation of amplitude and phase angle of elastic and shear moduli in frequency (ω_s) domain, it has been transformed to the time domain (t) using discrete inverse Fourier series transformation (IFFT) technique, as explained in Section 3.3.1. Fig. S25 (supplementary material) shows the variation of elastic and shear moduli in the time domain. All three elastic and shear moduli values at $t \to 0$ are almost equal to classical elastic and shear moduli without viscoelasticity effect. As time increases, the value of elastic and shear moduli relaxes and becomes constant after a certain time. A similar trend of elastic and shear moduli in the time-domain has also been reported by Endo and Pereira [96] for an orthotropic viscoelastic material. Furthermore, they also validated their Prony series computational model with experimental data obtained by the creep Test of material. A similar trend of time-dependent Young's modulus for isotropic material has also been observed by Jalocha [97] using a generalized Maxwell model.

In the next stage, the time-dependent variation of Young's moduli and shear moduli is utilized to obtain the time-dependent natural flexural frequency response of viscoelastic smart plates (a) and (b), as shown in Fig. 8. It is considered that the bottom

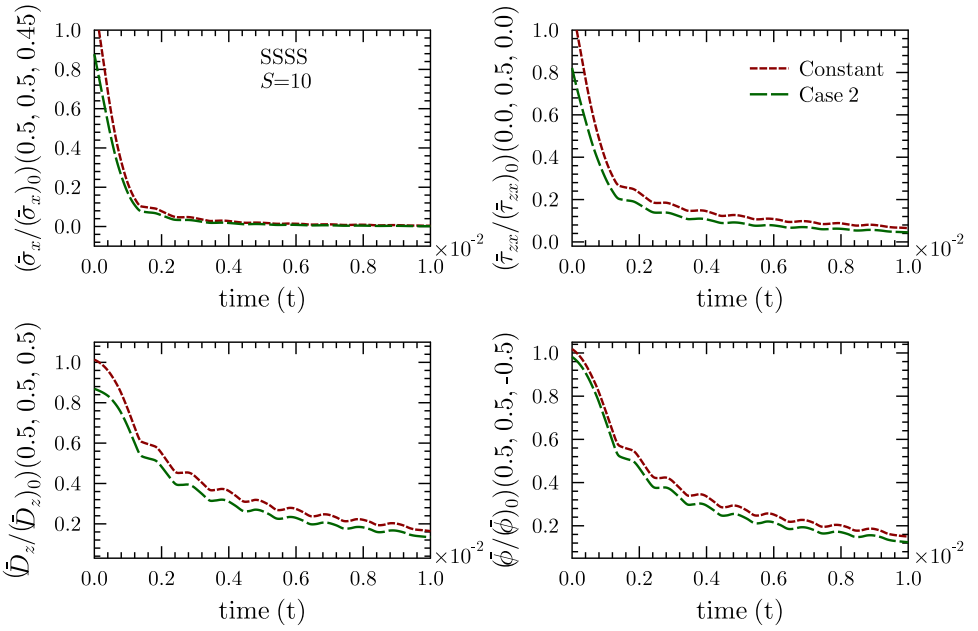

Fig. 10. Effect of viscoelasticity on the in-plane stress $\bar{\sigma}_x$, transverse stress $\bar{\sigma}_{zx}$, electric field $\bar{D}_z$ and electric potential $\bar{\phi}$ of three-layered moderately thick (S = 10) viscoelastic smart plate (a) with non-graded and graded properties. The time-dependent variation of in-plane stress $\bar{\sigma}_x$, transverse stress $\bar{\sigma}_{zx}$, electric field $\bar{D}_z$ and electric potential $\bar{\phi}$ is plotted in non-dimensionalized form for first vibration mode under SSSS boundary condition. The non-dimensionalized initial values of in-plane stress $(\bar{\sigma}_x)_0 = -5.8047$, transverse stress $(\bar{\sigma}_{zx})_0 = 0.53780$, electric field $(\bar{D}_z)_0 = 3.1374$ and electric potential $(\bar{\phi})_0 = -2.3274 \times 10^{-3}$ for non-viscous non-graded case are used for further normalization of the viscoelastic case.

surface of the IPFG viscoelastic smart plate is subjected to closed-circuit condition *i.e.* $\phi(x, y, -h/2) = 0$, and the top surface is under open circuit condition *i.e.* $D_z(x, y, h/2) = 0$. First, the effect of viscoelasticity on natural frequencies is studied for smart viscous plate (a) (plate without in-plane gradation) subjected to different mechanical boundary conditions. Fig. 9 shows the influence of viscoelasticity on the first five lowest natural frequencies of three-layered moderately thick (S = 10) viscoelastic smart plate (a) without graded properties.

The time-dependent variation of the first five lowest natural frequencies is plotted in non-dimensionalized form for different boundary conditions such as SSSS, CSSS, CCSS, CFSS. The non-dimensionalization is performed by dividing the flexural frequencies of the viscoelastic plate by the corresponding flexural frequency of elastic plate given in Table 7. It is observed that the viscoelastic layer acts as a damper. Due to viscoelastic behaviour of the composite layer, the natural frequencies of the smart hybrid plate are decreased with increasing time. It is worth noting that the natural frequencies decrease gradually with time, unlike viscoelastic properties, which decrease fast with the increase in time. The viscoelastic effect on lower vibration modes is more influenced by mechanical boundary conditions of the plates. The effect of viscoelasticity on higher mode natural frequencies is almost similar under all support conditions.

Fig. S26 (supplementary material) shows the effect of viscoelasticity on the first natural flexural frequencies of three-layered moderately thick (S = 10) inhomogeneous viscoelastic smart plate (b) having graded properties. The time-dependent variation of natural frequencies is plotted in non-dimensionalized form for different gradation cases under different edge conditions such as SSSS, CSSS, CCSS, CFSS. The non-dimensionalization is done by dividing the flexural frequencies of the viscoelastic plate by the flexural frequencies of the elastic plate without any gradation given in Table 7. It is found that the trend of viscoelastic effect on natural frequency is not affected much by inhomogeneity in composite layers, albeit the numerical values become different. For different gradation cases, the natural frequencies of the plate decrease with time in a similar pattern under all mechanical support conditions. Fig. 10 shows the influence of viscoelasticity on the in-plane stress $\bar{\sigma}_x$, transverse stress $\bar{\sigma}_{zx}$, electric field $\bar{D}_z$ and electric potential $\bar{\phi}$ of three-layered moderately thick (S = 10) viscoelastic smart plate (a) with non-graded and graded properties. The time-dependent variation of in-plane stress $\bar{\sigma}_x$, transverse stress $\bar{\sigma}_{zx}$, electric field $\bar{D}_z$ and electric potential $\bar{\phi}$ is plotted in non-dimensionalized form for first vibration mode under SSSS boundary condition. The non-dimensionalized initial values of in-plane stress $(\bar{\sigma}_x)_0 = -5.8047$, transverse stress $(\bar{\sigma}_{zx})_0 = 0.53780$, electric field $(\bar{D}_z)_0 = 3.1374$ and electric potential $(\bar{\phi})_0 = -2.3274 \times 10^{-3}$ for non-viscous non-graded case are used for further scaling of the viscoelastic case. It is observed that the stresses in the plate decrease fast with the increase in time and become constant after a certain value of time. Similar trend in time-dependent behaviour of stresses are observed under the gradation of properties and for the non-graded case, albeit with a difference in numerical values. The time-dependent behaviour of stresses is similar to time-dependent behaviours of viscoelastic properties like in Young's and shear moduli. However, electrical potential ($\bar{\phi}$) and electric field decrease ($\bar{D}_z$) gradually as time increases under both graded and non-graded case. It is also noted that the effect of gradation in elastic properties on electrical potential ($\bar{\phi}$) and electric field ($\bar{D}_z$) initially is very less but

increases significantly as time grows. This shows that the gradation of material properties in the presence of viscoelasticity alters the electric response of piezoelectric layers to a significant extent. In general, the numerical study considering viscoelastic behaviour demonstrates a potential time-dependent structural behaviour, which could be crucial for analysing the mechanical behaviour of a wide range of polymer composites accurately and prospective time-dependent programming in smart structural systems.

6. Conclusions and perspective

The influence of in-plane gradation of stiffness and density on the free-vibration response of hybrid piezoelectric Levy-type plate is investigated by developing an accurate analytical solution. Further, the coupled effect of viscoelasticity and gradation on the natural frequency response of the IPFG smart viscoelastic plates is studied. The displacement, stresses, and electrical variables are solved as the primary variable by developing Hamilton's principle-based mixed formulation. A power series approach is used in conjunction with the extended Kantorovich method and Fourier series to obtain the closed-form analytical solution for Levy-type support condition. Biot model, which corresponds to a standard linear viscoelastic model, is coupled with the analytical framework to implement the viscoelasticity of composite layers in the analysis. Although the present analytical solution is developed for the elastic and viscoelastic analysis of smart in-plane functionally graded rectangular plates, it is also directly applicable for the natural frequency analysis of the symmetric and asymmetric laminated piezoelectric viscoelastic/elastic plates of constant properties.

An extensive numerical study is performed to assess the effect of in-plane gradation and viscoelasticity of material properties on natural frequencies and mode shapes of hybrid FGM plates. The benchmark numerical results are tabulated for various gradation cases and configurations under different electrical and mechanical support conditions. Numerical results for homogenous piezoelectric elastic/viscoelastic plates are also reported as a special case of the present study. The current results are validated with the results available in the open literature and 3D FE results by performing separate numerical simulations. It is found that the present EKM-power series analytical model is very efficient and accurate in depicting the flexural frequencies and mode shapes of the hybrid FGM viscoelastic and elastic plates. Some of the most significant outcomes of this study are listed below.

- The in-plane gradation of stiffness and density in the elastic layers significantly alters the flexural frequencies of the hybrid intelligent plate. As material properties variation indexes increase, the flexural frequencies of the smart plate decrease remarkably. When the gradation indexes become doubled (from 0.5 to 1), the percentage decrement in natural frequencies is almost raised by 1.5 times. The effect of gradation on free vibration response significantly depends upon the type of mechanical support conditions.
- The influence of gradation in lower mode natural frequencies specifically depends on mechanical support conditions of the hybrid plate. Further, percentage decrement in first and lower mode natural frequencies is different for different support conditions, while the effect of gradation in higher mode frequencies shows less sensitivity to support conditions. The decrement in higher mode natural frequencies almost remains the same for all boundary conditions. Another interesting finding is that the influence of in-plane gradation on flexural frequencies is not affected much by the electrical circuit conditions of piezoelectric layers.
- The mode shapes of the IPFG smart plate are affected significantly due to in-plane variation of stiffness and density. The symmetric mode shapes of the plate can be made asymmetrical by introducing appropriate gradation.
- The stresses in the smart FGM plates are influenced remarkably by in-plane variation of material properties. It is found that as the gradation index increases, the stresses in the IPFG smart plate decrease. But displacements, electric field, and electrical potential are not significantly affected by the gradation of stiffness and density.
- Though the in-plane gradation of stiffness and density significantly affects the flexural frequencies of the smart hybrid plate, their effect on the electric voltage of the piezoelectric layer is considerably less. This observation can play a significant role in the design of sensors or actuators for vibration control applications.
- The current investigation shows that the desired electromechanical responses of hybrid IPFG plate can be obtained by controlling the in-plane variation of material properties in the elastic layers. Based on the proposed efficient and accurate numerical framework, further studies can be undertaken to simultaneously optimize multiple electrical and mechanical response parameters of interest in an expanded design space of layer-wise gradation parameters, material and geometric properties.
- For viscoelastic smart plates, the natural frequencies decrease gradually with time, whereas stresses in plate decrease fast and become constant after a critical time period. The decrement in electric response (in electric field and electric voltage) of the smart plate is also gradual. It is observed that the gradation of material properties in the presence of viscoelasticity significantly alters the electric response of piezoelectric layers. The presented numerical results demonstrate a great potential of the proposed viscoelastic analysis in the time domain for programming electromechanical responses of composite structures.
- Due to the consideration of viscoelastic effect, the natural frequencies decrease with time. The physical meaning of this variation is that the damping properties of viscoelastic layers diminish vibrational properties, while the damping behaviour mainly depends upon the type of boundary conditions. It is worth noting that the natural frequencies decrease gradually with time, unlike viscoelastic properties, which decrease fast with the increase in time. The viscoelastic effect on lower vibration modes is more influenced by mechanical boundary conditions of the plates. The effect of viscoelasticity on higher mode natural frequencies is almost similar under all support conditions.

The numerical study demonstrates a potential time-dependent electromechanical behaviour based on the present viscoelastic modelling coupled with in-plane gradation, which could be crucial for analysing the structural behaviour of a wide range of 'intelligent' polymer composites accurately and prospective temporal programming in smart structural systems. The analytical results provided in this paper will serve as benchmarks to validate numerical algorithms in applications of natural frequency analysis for elastic/viscoelastic piezoelectric plates with or without gradation. Furthermore, the present analytical solution approach can also be extended to obtain analytical solutions for bending and free vibration analysis of multi-directional functionally graded smart plates.

Declaration of competing interest

The authors declare that they have no known competing financial interests or personal relationships that could have appeared to influence the work reported in this paper.

Data availability

Data will be made available on request.

Acknowledgements

AS and TM would like to acknowledge the support received through the Science and Engineering Research Board, India (Grant no. SRG/2020/001398), India. SN acknowledges the initiation grant received from University of Southampton.

Appendix A. Supplementary data

Supplementary material related to this article can be found online at https://doi.org/10.1016/j.ymssp.2022.109636.

References

[1] F. Xu, X. Zhang, H. Zhang, A review on functionally graded structures and materials for energy absorption, Eng. Struct. 171 (2018) 309–325.
[2] P.S. Ghatage, V.R. Kar, P.E. Sudhagar, On the numerical modelling and analysis of multi-directional functionally graded composite structures: A review, Compos. Struct. 236 (2020) 111837.
[3] V. Birman, L.W. Byrd, Modeling and analysis of functionally graded materials and structures, Appl. Mech. Rev. 60 (5) (2007) 195–216.
[4] C.-P. Wu, K.-H. Chiu, Y.-M. Wang, et al., A review on the three-dimensional analytical approaches of multilayered and functionally graded piezoelectric plates and shells, Comput. Mater. Contin. 8 (2) (2008) 93–132.
[5] K. Swaminathan, D. Naveenkumar, A. Zenkour, E. Carrera, Stress, vibration and buckling analyses of FGM plates — A state-of-the-art review, Compos. Struct. 120 (2015) 10–31.
[6] P. Karsh, T. Mukhopadhyay, S. Dey, Stochastic dynamic analysis of twisted functionally graded plates, Composites B 147 (2018) 259–278.
[7] Vaishali T. Mukhopadhyay, P. Karsh, B. Basu, S. Dey, Machine learning based stochastic dynamic analysis of functionally graded shells, Compos. Struct. 237 (2020) 111870.
[8] P. Karsh, T. Mukhopadhyay, S. Dey, Stochastic low-velocity impact on functionally graded plates: Probabilistic and non-probabilistic uncertainty quantification, Composites B 159 (2019) 461–480.
[9] M.-C. Trinh, T. Mukhopadhyay, S.-E. Kim, A semi-analytical stochastic buckling quantification of porous functionally graded plates, Aerosp. Sci. Technol. 105 (2020) 105928.
[10] P. Karsh, T. Mukhopadhyay, S. Chakraborty, S. Naskar, S. Dey, A hybrid stochastic sensitivity analysis for low-frequency vibration and low-velocity impact of functionally graded plates, Composites B 176 (2019) 107221.
[11] A. Leissa, A. Martin, Vibration and buckling of rectangular composite plates with variable fiber spacing, Compos. Struct. 14 (4) (1990) 339–357.
[12] J. Tomar, D. Gupta, N. Jain, Free vibrations of an isotropic non-homogeneous infinite plate of parabolically varying thickness, Indian J. Pure Appl. Math 15 (2) (1984) 211–220.
[13] M. Fares, A. Zenkour, Buckling and free vibration of non-homogeneous composite cross-ply laminated plates with various plate theories, Compos. Struct. 44 (4) (1999) 279–287.
[14] D. Liu, C. Wang, W. Chen, Free vibration of FGM plates with in-plane material inhomogeneity, Compos. Struct. 92 (5) (2010) 1047–1051.
[15] T.-C. Yu, G.-J. Nie, Z. Zhong, F.-y. Chu, Analytical solution of rectangular plate with in-plane variable stiffness, Appl. Math. Mech. 34 (2013) 395–404.
[16] M. Amirpour, R. Das, E.S. Flores, Analytical solutions for elastic deformation of functionally graded thick plates with in-plane stiffness variation using higher order shear deformation theory, Composites B 94 (2016) 109–121.
[17] B. Uymaz, M. Aydogdu, S. Filiz, Vibration analyses of FGM plates with in-plane material inhomogeneity by Ritz method, Compos. Struct. 94 (4) (2012) 1398–1405.
[18] S. Yin, T. Yu, T.Q. Bui, X. Zheng, S. Tanaka, In-plane material inhomogeneity of functionally graded plates: A higher-order shear deformation plate isogeometric analysis, Composites B 106 (2016) 273–284.
[19] O.S. Hussein, S.B. Mulani, Reliability analysis and optimization of in-plane functionally graded cnt-reinforced composite plates, Struct. Multidiscip. Optim. 58 (3) (2018) 1221–1232.
[20] F. Chu, L. Wang, Z. Zhong, J. He, Hermite radial basis collocation method for vibration of functionally graded plates with in-plane material inhomogeneity, Comput. Struct. 142 (2014) 79–89.
[21] P. Malekzadeh, A. Alibeygi Beni, Nonlinear free vibration of in-plane functionally graded rectangular plates, Mech. Adv. Mater. Struct. 22 (8) (2015) 633–640.
[22] S. Yin, T. Yu, T.Q. Bui, X. Zheng, G. Yi, Rotation-free isogeometric analysis of functionally graded thin plates considering in-plane material inhomogeneity, Thin-Walled Struct. 119 (2017) 385–395.
[23] S. Kumar, A. Mitra, H. Roy, Large amplitude free vibration study of non-uniform plates with in-plane material inhomogeneity, Proc. Inst. Mech. Eng. L 232 (5) (2018) 371–387.
[24] S.-Y. Kuo, L.-C. Shiau, Buckling and vibration of composite laminated plates with variable fiber spacing, Compos. Struct. 90 (2) (2009) 196–200.

[25] V. Haciyev, A. Sofiyev, N. Kuruoglu, Free bending vibration analysis of thin bidirectionally exponentially graded orthotropic rectangular plates resting on two-parameter elastic foundations, Compos. Struct. 184 (2018) 372–377.
[26] Y. Xue, G. Jin, H. Ding, M. Chen, Free vibration analysis of in-plane functionally graded plates using a refined plate theory and isogeometric approach, Compos. Struct. 192 (2018) 193–205.
[27] M. Loja, J. Barbosa, In-plane functionally graded plates: A study on the free vibration and dynamic instability behaviours, Compos. Struct. 237 (2020) 111905.
[28] C. Lü, W. Chen, J. Shao, Semi-analytical three-dimensional elasticity solutions for generally laminated composite plates, Eur. J. Mech. A Solids 27 (5) (2008) 899–917.
[29] C. Lü, C.W. Lim, W. Chen, Semi-analytical analysis for multi-directional functionally graded plates: 3-D elasticity solutions, Internat. J. Numer. Methods Engrg. 79 (1) (2009) 25–44.
[30] A. Singh, P. Kumari, Two-dimensional elasticity solution for arbitrarily supported axially functionally graded beams, J. Solid Mech. 10 (4) (2018) 719–733.
[31] A. Singh, P. Kumari, Analytical solution of functionally graded beam having longitudinal stiffness variation, Int. J. Comput. Methods Eng. Sci. Mech. 19 (6) (2018) 390–395.
[32] A. Singh, P. Kumari, P. Bind, 2D free vibration solution of the hybrid piezoelectric laminated beams using extended kantorovich method, J. Inst. Eng India C 101 (1) (2020) 1–12.
[33] A. Singh, S. Kapuria, Analytical elasticity solution for accurate prediction of localized stresses in laminated composites under patch loading, Eur. J. Mech. A Solids 95 (2022) 104624.
[34] A. Singh, P. Kumari, R. Hazarika, Analytical solution for bending analysis of axially functionally graded angle-ply flat panels, in: Mathematical Problems in Engineering 2018.
[35] A. Singh, P. Kumari, Analytical free vibration solution for angle-ply piezolaminated plate under cylindrical bending: A piezo-elasticity approach, Adv. Comput. Des. 5 (1) (2020) 55–89.
[36] P. Kumari, A. Singh, R. Rajapakse, S. Kapuria, Three-dimensional static analysis of levy-type functionally graded plate with in-plane stiffness variation, Compos. Struct. 168 (2017) 780–791.
[37] A. Ravindran, K. Bhaskar, Three-dimensional analysis of composite FGM rectangular plates with in-plane heterogeneity, Int. J. Mech. Sci. 160 (2019) 386–396.
[38] A. Ravindran, K. Bhaskar, Elasticity solution for a sandwich plate having composite facesheets with in-plane grading, J. Sandw. Struct. Mater. (2020) 1099636220909810.
[39] P. Zhang, C. Qi, H. Fang, W. He, Three dimensional mechanical behaviors of in-plane functionally graded plates, Compos. Struct. 241 (2020) 112124.
[40] A. Singh, P. Kumari, Three-dimensional free vibration analysis of composite FGM rectangular plates with in-plane heterogeneity: An ekm solution, Int. J. Mech. Sci. 180 (2020) 105711.
[41] K. Asemi, M. Salehi, M. Akhlaghi, Three dimensional static analysis of two dimensional functionally graded plates, IJMECH 2 (2) (2013) 21–32.
[42] T. Xiang, S. Natarajan, H. Man, C. Song, W. Gao, Free vibration and mechanical buckling of plates with in-plane material inhomogeneity– a three dimensional consistent approach, Compos. Struct. 118 (2014) 634–642.
[43] Y. Huang, Y. Zhao, D. Cao, Bending and free vibration analysis of orthotropic in-plane functionally graded plates using a chebyshev spectral approach, Compos. Struct. 255 (2021) 112938.
[44] A. Singh, T. Mukhopadhyay, S. Adhikari, B. Bhattacharya, Voltage-dependent modulation of elastic moduli in lattice metamaterials: Emergence of a programmable state-transition capability, Int. J. Solids Struct. 208-209 (2021) 31–48.
[45] H. Madinei, H.H. Khodaparast, S. Adhikari, M. Friswell, Design of mems piezoelectric harvesters with electrostatically adjustable resonance frequency, Mech. Syst. Signal Process. 81 (2016) 360–374.
[46] S. Naskar, K.B. Shingare, S. Mondal, T. Mukhopadhyay, Flexoelectricity and surface effects on coupled electromechanical responses of graphene reinforced functionally graded nanocomposites: a unified size-dependent semi-analytical framework, Mech. Syst. Signal Process. 169 (2022) 108757.
[47] A. Singh, T. Mukhopadhyay, S. Adhikari, B. Bhattacharya, Active multi-physical modulation of poisson's ratios in composite piezoelectric lattices: on-demand sign reversal, Compos. Struct. 280 (2022) 114857.
[48] K.B. Shingare, S. Naskar, Probing the prediction of effective properties for composite materials, Eur. J. Mech. A Solids 87 (2022) 104228.
[49] G. Martínez-Ayuso, M.I. Friswell, H.H. Khodaparast, J.I. Roscow, C.R. Bowen, Electric field distribution in porous piezoelectric materials during polarization, Acta Mater. 173 (2019) 332–341.
[50] W. Chen, H. Ding, On free vibration of a functionally graded piezoelectric rectangular plate, Acta Mech. 153 (3) (2002) 207–216.
[51] P. Lu, H. Lee, C. Lu, Exact solutions for simply supported functionally graded piezoelectric laminates by Stroh-like formalism, Compos. Struct. 72 (3) (2006) 352–363.
[52] S. Brischetto, E. Carrera, Refined 2d models for the analysis of functionally graded piezoelectric plates, J. Intell. Mater. Syst. Struct. 20 (15) (2009) 1783–1797.
[53] A. Zenkour, R. Alghanmi, Stress analysis of a functionally graded plate integrated with piezoelectric faces via a four-unknown shear deformation theory, Results Phys. 12 (2019) 268–277.
[54] S.-Q. Zhang, G.-Z. Zhao, M.N. Rao, R. Schmidt, Y.-J. Yu, A review on modeling techniques of piezoelectric integrated plates and shells, J. Intell. Mater. Syst. Struct. 30 (8) (2019) 1133–1147.
[55] P. Zhang, C. Qi, H. Fang, X. Sun, A semi-analytical approach for the flexural analysis of in-plane functionally graded magneto-electro-elastic plates, Compos. Struct. 250 (2020) 112590.
[56] P. Zhang, C. Qi, X. Sun, H. Fang, Y. Huang, Bending behaviors of the in-plane bidirectional functionally graded piezoelectric material plates, Mech. Adv. Mater. Struct. (2020) 1–21.
[57] P. Zhang, C. Qi, H. Fang, X. Sun, Free vibration analysis of functionally graded magneto-electro-elastic plates with in-plane material heterogeneity, J. Intell. Mater. Syst. Struct. (2020) 1045389X20975487.
[58] J. Zhang, G. Zheng, The biot model and its application in viscoelastic composite structures, J. Vib. Acoust. 129 (5) (2007) 533–540.
[59] M.-y. Hu, A.-w. Wang, Free vibration and transverse stresses of viscoelastic laminated plates, Appl. Math. Mech. 30 (1) (2009) 101.
[60] Y. Mao, Y. Fu, H. Dai, Creep buckling and post-buckling analysis of the laminated piezoelectric viscoelastic functionally graded plates, Eur. J. Mech. A Solids 30 (4) (2011) 547–558.
[61] A. Zenkour, Bending responses of an exponentially graded simply-supported elastic/viscoelastic/elastic sandwich plate, Acta Mech. Solida Sin. 24 (3) (2011) 250–261.
[62] Y. Wang, Z. Wang, L. Zu, Stability of viscoelastic rectangular plate with a piezoelectric layer subjected to follower force, Arch. Appl. Mech. 83 (4) (2013) 495–507.
[63] A. Alibeigloo, Effect of viscoelastic interface on three-dimensional static and vibration behavior of laminated composite plate, Composites B 75 (2015) 17–28.
[64] P. Wu, D. Zhou, W. Liu, W. Lu, L. Wan, Three-dimensional elasticity solution of layered plates with viscoelastic interlayers, Mech. Time-Depend. Mater. 21 (3) (2017) 307–329.
[65] M. Wang, Z. Yang, P. Wu, H. Fang, R. Huo, 3D analytical solution for multilayer functionally graded plates with viscoelastic interlayers, Mech. Based Des. Struct. Mach. (2021) 1–20.

[66] K.R. Karim, G. Chen, Surface damping effect of anchored constrained viscoelastic layers on the flexural response of simply supported structures, Mech. Syst. Signal Process. 27 (2012) 419–432.
[67] S.C. Kattimani, M. Ray, Vibration control of multiferroic fibrous composite plates using active constrained layer damping, Mech. Syst. Signal Process. 106 (2018) 334–354.
[68] J.S. Moita, A.L. Araújo, V.F. Correia, C.M.M. Soares, J. Herskovits, Active-passive damping in functionally graded sandwich plate/shell structures, Compos. Struct. 202 (2018) 324–332.
[69] F. Mastroddi, F. Martarelli, M. Eugeni, C. Riso, Time-and frequency-domain linear viscoelastic modeling of highly damped aerospace structures, Mech. Syst. Signal Process. 122 (2019) 42–55.
[70] A. Batou, S. Adhikari, Optimal parameters of viscoelastic tuned-mass dampers, J. Sound Vib. 445 (2019) 17–28.
[71] W. Sun, Z. Wang, X. Yan, M. Zhu, Inverse identification of the frequency-dependent mechanical parameters of viscoelastic materials based on the measured FRFs, Mech. Syst. Signal Process. 98 (2018) 816–833.
[72] P. Grosso, A. De Felice, S. Sorrentino, A method for the experimental identification of equivalent viscoelastic models from vibration of thin plates, Mech. Syst. Signal Process. 153 (2021) 107527.
[73] A. Singh, P. Kumari, Two-dimensional free vibration analysis of axially functionally graded beams integrated with piezoelectric layers: An piezoelasticity approach, Int. J. Appl. Mech. 12 (04) (2020) 2050037.
[74] T. Mukhopadhyay, S. Adhikari, A. Batou, Frequency domain homogenization for the viscoelastic properties of spatially correlated quasi-periodic lattices, Int. J. Mech. Sci. 150 (2019) 784–806.
[75] D.I. Jones, HandBook of Viscoelastic Vibration Damping, John Wiley & Sons, 2001.
[76] R. Christensen, Theory of Viscoelasticity: An Introduction, Elsevier, 2012.
[77] P.A.M. Dirac, et al., The Principles of Quantum Mechanics, no. 27, Oxford University Press, 1981.
[78] L. Rouleau, J.-F. Deü, A. Legay, F. Le Lay, Application of Kramers–Kronig relations to time–temperature superposition for viscoelastic materials, Mech. Mater. 65 (2013) 66–75.
[79] H. Booij, G. Thoone, Generalization of kramers-kronig transforms and some approximations of relations between viscoelastic quantities, Rheol. Acta 21 (1) (1982) 15–24.
[80] L. Xi, R. Luo, Use of Kramers–Kronig relations to construct the master curves of asphalt materials, Mater. Struct. 54 (1) (2021) 1–16.
[81] M. Enelund, P. Olsson, Damping described by fading memory—analysis and application to fractional derivative models, Int. J. Solids Struct. 36 (7) (1999) 939–970.
[82] M.A. Biot, Variational principles in irreversible thermodynamics with application to viscoelasticity, Phys. Rev. 97 (6) (1955) 1463.
[83] R.L. Bagley, P.J. Torvik, Fractional calculus-a different approach to the analysis of viscoelastically damped structures, AIAA J. 21 (5) (1983) 741–748.
[84] G.A. Lesieutre, D.L. Mingori, Finite element modeling of frequency-dependent material damping using augmenting thermodynamic fields, J. Guid. Control Dyn. 13 (6) (1990) 1040–1050.
[85] D.J. McTavish, P.C. Hughes, Modeling of linear viscoelastic space structures, ASME, J. Vib. Acoust. 115 (1) (1993) 103–110.
[86] S. Adhikari, Energy Dissipation in Vibrating Structures, First Year Report, Cambridge University Engineering Department, Cambridge, UK.
[87] S. Adhikari, J. Woodhouse, Identification of damping: Part 1, viscous damping, J. Sound Vib. 243 (1) (2001) 43–61.
[88] M.A. Ezzat, H.M. Youssef, Three-dimensional thermo-viscoelastic material, Mech. Adv. Mater. Struct. 23 (1) (2016) 108–116.
[89] K. Barrett, A. Gotts, Fem for one-and two-dimensional viscoelastic materials with spherical and rotating domains using FFT, Comput. Struct. 82 (2–3) (2004) 181–192.
[90] R.M. Gray, J.W. Goodman, Fourier Transforms: An Introduction for Engineers, vol. 322, Springer Science & Business Media, 2012.
[91] P. Kumari, A. Singh, Three-dimensional analytical solution for FGM plate with varying material properties in in-plane directions using extended kantorovich method, in: Recent Advances in Structural Engineering, vol. 1, Springer, 2019, pp. 611–621.
[92] S. Behera, P. Kumari, Analytical piezoelasticity solution for natural frequencies of levy-type piezolaminated plates, Int. J. Appl. Mech. 11 (03) (2019) 1950023.
[93] S. Kapuria, G. Achary, A coupled zigzag theory for the dynamics of piezoelectric hybrid cross-ply plates, Arch. Appl. Mech. 75 (1) (2005) 42–57.
[94] P. Heyliger, D. Saravanos, Exact free-vibration analysis of laminated plates with embedded piezoelectric layers, J. Acoust. Soc. Am. 98 (3) (1995) 1547–1557.
[95] S. Malekmohammadi, B. Tressou, C. Nadot-Martin, F. Ellyin, R. Vaziri, Analytical micromechanics equations for elastic and viscoelastic properties of strand-based composites, J. Compos. Mater. 48 (15) (2014) 1857–1874.
[96] V.T. Endo, J.C. de Carvalho Pereira, Linear orthotropic viscoelasticity model for fiber reinforced thermoplastic material based on prony series, Mech. Time-Depend. Mater. 21 (2) (2017) 199–221.
[97] D. Jalocha, A. Constantinescu, R. Neviere, Revisiting the identification of generalized maxwell models from experimental results, Int. J. Solids Struct. 67 (2015) 169–181.